Projective and Telescopic Projective Integration for Non-Linear Kinetic Mixtures

Rafael Bailo, Thomas Rey

Projective and Telescopic Projective Integration for Non-Linear Kinetic Mixtures

Rafael Bailo and Thomas Rey

Univ. Lille, CNRS, Inria, UMR 8524 - Laboratoire Paul Painlevé
F-59000 Lille, France
rafael.bailo@univ-lille.fr
thomas.rey@univ-lille.fr

Abstract

We propose fully explicit projective integration and telescopic projective integration schemes for the multispecies Boltzmann and Bhatnagar-Gross-Krook (BGK) equations. The methods employ a sequence of small forward-Euler steps, intercalated with large extrapolation steps. The telescopic approach repeats said extrapolations as the basis for an even larger step. This hierarchy renders the computational complexity of the method essentially independent of the stiffness of the problem, which permits the efficient solution of equations in the hyperbolic scaling with very small Knudsen numbers. We validate the schemes on a range of scenarios, demonstrating its prowess in dealing with extreme mass ratios, fluid instabilities, and other complex phenomena.

AMS Subject Classification — 65M08; 65M12; 76P05; 82C40.

Keywords — Multispecies gas; kinetic mixture; Boltzmann equation; BGK model; projective integration; Sod Tube; Kelvin-Helmholtz; Richtmyer-Meshkov.

1 Introduction

Mixtures of rarefied gases are found in a wide variety of systems, ranging from the re-entry of an interplanetary probe in the upper atmosphere [21] to microscale flows in pumps which use no moving parts (viz. the Knudsen compressor, [35]). Such complex gases cannot be described by classical fluid models, such as the compressible Euler or the Navier-Stokes systems, because of their non-equilibrium behaviour, induced by their rarefaction. Kinetic models, such as the seminal Boltzmann equation, are thus favoured to describe these systems because they are able to reflect the non-equilibrium character of the gases, retaining information about the microscopic many-particle dynamics while avoiding the sheer complexity of the microscopic approach. Furthermore, actual gases are usually a mixture of different chemical species; for instance, the chemistry of the upper atmosphere is made of up to 20 different species (mostly recombinations of O_2, CO_2, H_2, and CH_4). The realistic simulations of such systems must involve multispecies kinetic models.

Whereas the mathematical properties of the classical Boltzmann equation for a single species gas are well known by now (crucially, its derivation from Newtonian dynamics was addressed in [27]), many questions remain open for the multispecies case. The most recent theoretical results on the topic come from the series of papers [9, 10]; they prove the existence, uniqueness,

positivity, and exponential trend to equilibrium for the full non-linear multispecies Boltzmann equation in a perturbative, polynomially-weighted, and isotropic $L^1_v L^\infty_x$ setting. The case of the unperturbed setting remains mostly open.

At the numerical level, the most advanced deterministic methods use a Fourier approach to evaluate the full collision operator: a fast spectral algorithm was recently introduced in [59] for the multispecies case. Nevertheless, the method was not asymptotic preserving (AP), namely, stable in the small relaxation parameter limit; the only recent paper on this subject can be found in [7], where the Maxwell-Stephan limit for a multispecies gas is investigated numerically via a moment method (which does not compute the full operator). In this work, we shall introduce a new family of numerical integrators for full kinetic multispecies models that are able to deal with a large range of values of the relaxation parameters uniformly on the numerical parameters.

Projective integration (PInt) is a robust and fully explicit method that allows for the time integration of (two-scale) stiff systems with arbitrary order of accuracy in time. The method was first proposed in [29] for stiff systems of ordinary differential equations with a clear gap in their eigenvalue spectrum. In such problems, the fast modes, corresponding to the Jacobian eigenvalues with large negative real parts, decay quickly; it is the slow modes, related to eigenvalues of smaller magnitude, that are of practical interest. In this regime, PInt permits a stable yet explicit integration by combining small and large steps. The integrator performs a few small (inner) steps of an explicit method, using a step size δt , until the transients corresponding to the fast modes have decayed; subsequently, the solution is projected (extrapolated) forward in time over a large (outer) time step of size $\Delta t \gg \delta t$.

PInt was analysed for kinetic equations with a diffusive scaling in [39]. An arbitrary order version, based on Runge-Kutta methods, has been proposed recently in [37], where it was also analysed for kinetic equations in the advection-diffusion limit. In [38], the scheme was used to construct a explicit, flexible, arbitrary order method for general non-linear hyperbolic conservation laws, based on their relaxation to a kinetic equation. Alternative approaches to obtain higher-order PInt schemes have been proposed in [40, 50]. These methods align with recent research efforts on numerical methods for multiscale simulation [25, 28].

For problems exhibiting more than two time scales, telescopic projective integration (TPInt) was proposed in [30]. In these methods, the projective idea is applied recursively. Starting from an inner integrator at the fastest time scale, a PInt method is constructed with a time step that corresponds to the second-fastest scale. This PInt method is then considered as the inner integrator of yet another PInt method at a coarser level. By repeating as required, TPInt methods construct a hierarchy of projective levels, each using the previous one as its inner step. This idea was explored for linear kinetic equations in [47]. These methods turn out to have a computational cost that is essentially independent of the stiffness of the collision operator. This property was used with great success in the series of papers [45, 46] to develop PInt and TPInt methods for the full non-linear Bhatnagar-Gross-Krook (BGK) and Boltzmann equations of single-species rarefied gas dynamics.

PInt methods are not asymptotic preserving (AP) methods as such, because the schemes cannot be evaluated explicitly at $\varepsilon = 0$ to obtain a classical numerical scheme for the limiting equation. Nevertheless, PInt and TPInt methods share important features with AP methods. In particular, their computational cost does (in many cases) not depend on the stiffness of the problem. To be precise, it was shown in [47] for linear kinetic equations that the number of inner time steps at each level of the telescopic hierarchy is independent of the small-scale parameter

ε, as is the step size of the outermost integrator. The only parameter in the method which may depend on ε is the number of levels in the telescopic hierarchy. For systems in which the spectrum of the collision operator falls apart into a set of clearly separate clusters (each corresponding to a specific time scale), the number of levels equals the number of spectral clusters. In this regime, the computational cost is completely independent from ε. When the collision operator comprises a continuum of time scales, the number of TPInt levels increases logarithmically with ε.

The linearisation of the multispecies Boltzmann operator around its equilibria has very similar properties to the classical single species Boltzmann operator, as shown in [20, 10]. Among others, its spectrum is well separated, with slow modes close to the origin, fast modes at a distance of order ε^{-1} left of the imaginary axis, and an essential part even farther away from the axis [24, 49]; this information was the basis for the development of the TPInt method in [46]. The spectral gap estimates in the multispecies setting are also very similar to the single species case. In this paper, we will exploit this structure to develop a TPInt method for the multispecies Boltzmann equation.

The rest of the work is organised as follows. In Section 2 we recall the elements of kinetic theory before presenting the models under consideration: the multispecies Boltzmann and BGK equations. Section 3 develops the numerical schemes which we shall use to study these models, with emphasis on the novelty of this paper: the use of projective integration and telescopic projective integration to construct uniformly accurate schemes for the multispecies BGK model. In Section 4 we compute the approximate spectrum of the numerical scheme and discuss the strategy for the choice of the parameters of the numerical methods. Finally, Section 5 presents a variety of numerical experiments, both in $1+1$ and $2+2$ dimensions of the phase space, which demonstrate how the schemes can handle extreme mass ratios, fluid instabilities, and other complex phenomena.

2 On Kinetic Equations and Multiple Species Models

The cornerstone of kinetic theory is the Boltzmann equation, which describes the evolution in time of the distribution of the particles of a rarefied gas. Each particle is subject to ballistic motion, travelling in a straight line at a given velocity, which may only change when it collides with another particle. These collisions are assumed to take place instantaneously and to conserve momentum and kinetic energy. Moreover, the gas is assumed to be dilute enough so that collisions between three or more particles can be neglected.

The *distribution* of particles, $f^\varepsilon(t, \mathbf{x}, \mathbf{v})$, is a non-negative function which describes for every time t the likelihood of finding a particle at a given position $\mathrm{d}\mathbf{x}$, with a given velocity $\mathrm{d}\mathbf{v}$. In this work, f^ε is understood in the *number* sense, meaning it is not a probability measure. To be precise[1], $\iint f^\varepsilon(t, \mathbf{x}, \mathbf{v})\,\mathrm{d}\mathbf{x}\,\mathrm{d}\mathbf{v} = N$ for all times $t \geq 0$, where N is the number of particles in the gas. All particles are assumed identical, each with mass $m > 0$.

[1] All the integrals in the text are taken over the full position domain, the full velocity domain, or the entire domain of Equation (2.1), unless otherwise stated:

$$\int \mathrm{d}\mathbf{x} \equiv \int_\Omega \mathrm{d}\mathbf{x}, \quad \int \mathrm{d}\mathbf{v} \equiv \int_{\mathbb{R}^{D_\mathbf{v}}} \mathrm{d}\mathbf{v}, \quad \iint \mathrm{d}\mathbf{x}\,\mathrm{d}\mathbf{v} \equiv \iint_{\Omega\times\mathbb{R}^{D_\mathbf{v}}} \mathrm{d}\mathbf{x}\,\mathrm{d}\mathbf{v}.$$

The distribution f^ε evolves according to the kinetic equation

$$\begin{cases} \partial_t f^\varepsilon + \mathbf{v}\cdot\nabla_{\mathbf{x}} f^\varepsilon = \dfrac{1}{\varepsilon}\mathcal{Q}[f^\varepsilon], \quad \mathbf{x}\in\Omega\subseteq\mathbb{R}^{D_{\mathbf{x}}},\ \mathbf{v}\in\mathbb{R}^{D_{\mathbf{v}}},\ t>0, \\ f^\varepsilon(0,\mathbf{x},\mathbf{v}) = f_0(\mathbf{x},\mathbf{v}), \end{cases} \tag{2.1}$$

posed with appropriate boundary conditions. This equation couples a *transport operator*, which models the displacement of particles, with a *collision operator* $\mathcal{Q}$, which describes the changes in momentum due to collisions. In this work, $D_{\mathbf{x}} = D_{\mathbf{v}} = 1$ or 2.

The frequency of collisions is governed by the *Knudsen number* ε, a measure of the average distance that a particle can travel before colliding with another one. The value of ε distinguishes the *kinetic regime*, where collisions are rare, from the *hydrodynamic regime*, where collisions dominate the dynamics; the former corresponds to larger values of ε, and the latter, to smaller values.

The seminal Boltzmann collision operator $\mathcal{Q}$ is a quadratic operator local in $(t,\mathbf{x})$. The time and position act only as parameters in $\mathcal{Q}$ and therefore will be omitted in its description. It is given, for $D_{\mathbf{v}}\geq 2$, by

$$\mathcal{Q}[f](\mathbf{v}) = \iint_{\mathbb{R}^{D_{\mathbf{v}}}\times\mathbb{S}^{D_{\mathbf{v}}-1}} B(|\mathbf{v}-\mathbf{v}_*|,\cos\theta)\ (f'f'_* - ff_*)\,\mathrm{d}\mathbf{v}_*\,\mathrm{d}\sigma, \tag{2.2}$$

where we have used the shorthand $f = f(\mathbf{v})$, $f_* = f(\mathbf{v}_*)$, $f' = f(\mathbf{v}')$, $f'_* = f(\mathbf{v}'_*)$. The velocities of the colliding pairs, $(\mathbf{v},\mathbf{v}_*)$ and $(\mathbf{v}',\mathbf{v}'_*)$, can be parametrized as

$$\mathbf{v}' = \frac{\mathbf{v}+\mathbf{v}_*}{2} + \frac{|\mathbf{v}-\mathbf{v}_*|}{2}\sigma, \qquad \mathbf{v}'_* = \frac{\mathbf{v}+\mathbf{v}^*}{2} - \frac{|\mathbf{v}-\mathbf{v}_*|}{2}\sigma.$$

The collision kernel B is a non-negative function which, by physical arguments of invariance, may only depend on $|\mathbf{v}-\mathbf{v}_*|$ and $\cos\theta = \hat{g}\cdot\sigma$ (where $\hat{g} = (\mathbf{v}-\mathbf{v}_*)/|\mathbf{v}-\mathbf{v}_*|$). It characterises the details of the binary interactions, and has the form

$$B(|\mathbf{v}-\mathbf{v}_*|,\cos\theta) = |\mathbf{v}-\mathbf{v}_*|\,\Phi(|\mathbf{v}-\mathbf{v}_*|,\cos\theta). \tag{2.3}$$

The scattering cross-section Φ, in the case of inverse k^{th} power forces between particles, can be written as

$$\Phi(|\mathbf{v}-\mathbf{v}_*|,\cos\theta) = b_\alpha(\cos\theta)\,|\mathbf{v}-\mathbf{v}_*|^{\alpha-1},$$

with $\alpha = (k-5)/(k-1)$. The special situation $k=5$ gives the so-called Maxwell pseudo-molecules model with $B(|\mathbf{v}-\mathbf{v}_*|,\cos\theta) = b_0(\cos\theta)$. For the Maxwell case the collision kernel is independent of the relative velocity. For numerical purposes, a widely used model is the variable hard sphere (VHS) model introduced by Bird [5]. The model corresponds to $b_\alpha(\cos\theta) = C_\alpha$, where C_α is a positive constant, and hence $\Phi(|\mathbf{v}-\mathbf{v}_*|,\cos\theta) = C_\alpha|\mathbf{v}-\mathbf{v}_*|^{\alpha-1}$. For further details on the physical background and derivation of the Boltzmann equation, we refer to [16, 57]

Equation (2.1) is rich with structural properties. In terms of conservation, its weak form reveals that any conserved quantity of the dynamics corresponds to an associated *collision in-*

variant of $\mathcal{Q}$: a function $\varphi(\mathbf{v})$ such that

$$\int \mathcal{Q}[f](\mathbf{v})\,\varphi(\mathbf{v})\,\mathrm{d}\mathbf{v} = 0$$

for any function $f(\mathbf{v})$. For the Boltzmann operator, the space of collision invariants is given by $\mathrm{span}\{1, \mathbf{v}, |\mathbf{v}|^2\}$ [15]. In consequence, the *mass*, *momentum*, and *kinetic energy* of the distribution, respectively $\iint m f^\varepsilon(t,\mathbf{x},\mathbf{v})\,\mathrm{d}\mathbf{x}\,\mathrm{d}\mathbf{v}$, $\iint m\mathbf{v} f^\varepsilon(t,\mathbf{x},\mathbf{v})\,\mathrm{d}\mathbf{x}\,\mathrm{d}\mathbf{v}$, and $\iint \frac{m}{2}|\mathbf{v}|^2 f^\varepsilon(t,\mathbf{x},\mathbf{v})\,\mathrm{d}\mathbf{x}\,\mathrm{d}\mathbf{v}$, are conserved.

In terms of dynamics, the relaxation properties of Eq. (2.1) are well-understood. The celebrated H-theorem characterises the dissipation of the *Boltzmann entropy*,

$$\mathcal{H} = \int f^\varepsilon(\mathbf{v}) \log(f^\varepsilon(\mathbf{v}))\,\mathrm{d}\mathbf{v}.$$

At the local level, the theorem states

$$\mathcal{S} = \int \mathcal{Q}[f^\varepsilon](\mathbf{v}) \log(f^\varepsilon(\mathbf{v}))\,\mathrm{d}\mathbf{v} \leq 0, \tag{2.4}$$

where $\frac{\partial \mathcal{H}}{\partial t} + \nabla_{\mathbf{x}} \cdot \mathcal{J} = \frac{\mathcal{S}}{\varepsilon}$ and $\mathcal{J} = \int \mathbf{v} f^\varepsilon(\mathbf{v}) \log(f^\varepsilon(\mathbf{v}))\,\mathrm{d}\mathbf{v}$, see, for instance, [14, 16]. Furthermore, the equality in (2.4) is only achieved for states in the kernel of $\mathcal{Q}$. Such equilibrium states are always Maxwellian distributions:

$$f^\varepsilon = \mathcal{M}^{n,\bar{\mathbf{v}},T}(t,\mathbf{x},\mathbf{v}) := n(t,\mathbf{x}) \left(\frac{m}{2\pi T}\right)^{D_{\mathbf{v}}/2} \exp\left(-\frac{m(\bar{\mathbf{v}}-\mathbf{v})^2}{2T}\right)$$

for particles of mass m. The *number density* n, the *mass density* ρ, the *average velocity* $\bar{\mathbf{v}}$, the *temperature* T, and the *pressure* $\mathcal{P}$ are (local) moments computed from the distribution which depend only on time and position; they are given by

$$n = \int f^\varepsilon\,\mathrm{d}\mathbf{v}, \quad \rho = mn, \quad \rho\bar{\mathbf{v}} = \int m\mathbf{v} f^\varepsilon\,\mathrm{d}\mathbf{v}, \quad \frac{D_{\mathbf{v}}}{2} nT = \int \frac{m}{2}|\bar{\mathbf{v}}-\mathbf{v}|^2 f^\varepsilon\,\mathrm{d}\mathbf{v}, \tag{2.5}$$

where $\rho = mn$ and $\mathcal{P} = nT$. Note, in particular, that the Maxwellian $\mathcal{M}^{n,\bar{\mathbf{v}},T}$ has moments $n, \bar{\mathbf{v}}, T$.

2.1 The Bhatnagar-Gross-Krook (BGK) Model

The collision operator (2.2) has a complicated structure from both the analytical and the numerical perspectives. Because of this, many works have proposed simpler operators which attempt to capture some or all of the structural properties of $\mathcal{Q}$. A ubiquitous simplification is the model of Bhatnagar-Gross-Krook [4]; since the overall effect of the Boltzmann operator is to drive f^ε towards the corresponding Maxwellian, they propose a reduced operator which makes the relaxation explicit:

$$\mathcal{Q}^{\mathrm{BGK}}[f^\varepsilon] = \nu(\mathcal{M}[f^\varepsilon] - f^\varepsilon), \tag{2.6}$$

where $\mathcal{M}[f^\varepsilon]$ is the Maxwellian whose moments $n, \bar{\mathbf{v}}, T$ are the ones of f^ε, and where $\nu(t, \mathbf{x})$ is a positive collision rate to be determined. This simplification can be derived from $\mathcal{Q}$ by assuming that the distribution f^ε is already close to equilibrium. The BGK equation is thus defined as the evolution law (2.1) together with the operator (2.6).

Despite its apparent simplicity, the BGK model captures many structural aspects of the Boltzmann collision operator. Because $\mathcal{M}[f^\varepsilon]$ and f^ε share the first three moments, the invariants of $\mathcal{Q}$ are also invariants of $\mathcal{Q}^{\mathrm{BGK}}$ whenever the collision rate does not depend on $\mathbf{v}$. Therefore, the new dynamics conserve the mass, momentum, and kinetic energy of f^ε as well. The dynamical structure of $\mathcal{Q}$ is also preserved by the BGK model because the H-theorem still holds:

$$\mathcal{S} = \int \mathcal{Q}^{\mathrm{BGK}}[f^\varepsilon](\mathbf{v}) \log(f^\varepsilon(\mathbf{v}))\, \mathrm{d}\mathbf{v} \leq 0,$$

see, for instance, [54]. Once again, the equality is only achieved by the equilibrium states, which are the Maxwellians by construction.

2.2 The Multispecies Boltzmann Equation

A limitation of the Boltzmann equation (2.1) is the assumption that all gas particles are identical. However, it is possible to extend this equation to the case of a mixture of gases by the physical arguments used in the single species case [8]. As stated in the introduction, the derivation of the multispecies Boltzmann equation is mostly formal, unlike that of the single species case, which has been clearly established in a variety of works such as [27].

We will consider a mixture of P species, each described by a distribution[2] $f_p(t, \mathbf{x}, \mathbf{v})$, a time-dependent non-negative function as before. Each distribution is understood in the number sense:

$$\iint f_p(t, \mathbf{x}, \mathbf{v})\, \mathrm{d}\mathbf{x}\, \mathrm{d}\mathbf{v} = N_p$$

for all times $t \geq 0$, where N_p is the number of particles in the p^{th} species. All particles of that species are assumed identical, each with mass m_p.

The distributions f_p evolve according to the so-called multispecies Boltzmann equation, given by

$$\begin{cases} \partial_t f_p + \mathbf{v} \cdot \nabla_{\mathbf{x}} f_p = \dfrac{1}{\varepsilon} \mathcal{Q}_p[\boldsymbol{f}], \quad \mathbf{x} \in \Omega \subseteq \mathbb{R}^{D_{\mathbf{x}}}, \, \mathbf{v} \in \mathbb{R}^{D_{\mathbf{v}}}, \, t > 0, \\ \mathcal{Q}_p[\boldsymbol{f}] = \displaystyle\sum_{q=1}^{P} \mathcal{Q}_{p,\,q}[f_p, f_q], \\ f_p(0, \mathbf{x}, \mathbf{v}) = f_{p,\,0}(\mathbf{x}, \mathbf{v}), \end{cases} \tag{2.7}$$

posed with appropriate boundary conditions. The changes of momentum of the p^{th} species are now governed by a sum of collision operators, one for each species in the gas. These multispecies collision operators $\mathcal{Q}_{p,\,q}$ are similar to the classical Boltzmann operator (2.2); namely, they are

[2] The ε notation is dropped in the interest of simplicity. Henceforth, f stands for f^ε.

given by

$$\mathcal{Q}_{p,\,q}[f_p, f_q] = \iint_{\mathbb{R}^{D_\mathbf{v}}\times\mathbb{S}^{D_\mathbf{v}-1}} B_{p,\,q}(|\mathbf{v}-\mathbf{v}_*|, \cos\theta)\left[f_p\left(\mathbf{v}'\right) f_q\left(\mathbf{v}'_*\right) - f_p(\mathbf{v})\, f_q(\mathbf{v}_*)\right] \mathrm{d}\mathbf{v}_* \,\mathrm{d}\sigma, \quad (2.8)$$

where inter-species collisions are given by

$$\begin{aligned} \mathbf{v}' &= \frac{1}{m_p+m_q}\left(m_p\mathbf{v} + m_q\mathbf{v}_* + m_q|\mathbf{v}-\mathbf{v}_*|\sigma\right), \\ \mathbf{v}'_* &= \frac{1}{m_p+m_q}\left(m_p\mathbf{v} + m_q\mathbf{v}_* - m_p|\mathbf{v}-\mathbf{v}_*|\sigma\right). \end{aligned} \quad (2.9)$$

Note that in the intra-species collision case $p = q$, (2.8) corresponds to the classical Boltzmann operator (2.2). We shall also assume for the sake of simplicity that the inter-species collision kernel $B_{p,\,q}$ is independent on p and q, and equal to the variable hard spheres kernel (2.3).

The conservation properties of the Boltzmann equation persist in the multispecies case at the level of the mixture. The mass of each species, $\iint m_p f_p(t,\mathbf{x},\mathbf{v})\,\mathrm{d}\mathbf{x}\,\mathrm{d}\mathbf{v}$, is conserved because 1 remains an invariant of each operator:

$$\int \mathcal{Q}_{p,\,q}[f,g](\mathbf{v})\,\mathrm{d}\mathbf{v} = 0$$

for any functions $f(\mathbf{v})$ and $g(\mathbf{v})$. However, the functions $\mathbf{v}$ and $|\mathbf{v}|^2$ are only invariants in the sense that

$$\int \mathbf{v}\mathcal{Q}_{p,\,q}[f,g](\mathbf{v})\,\mathrm{d}\mathbf{v} = -\int \mathbf{v}\mathcal{Q}_{q,\,p}[g,f](\mathbf{v})\,\mathrm{d}\mathbf{v} \quad (2.10)$$

and

$$\int |\mathbf{v}|^2\mathcal{Q}_{p,\,q}[f,g](\mathbf{v})\,\mathrm{d}\mathbf{v} = -\int |\mathbf{v}|^2\mathcal{Q}_{q,\,p}[g,f](\mathbf{v})\,\mathrm{d}\mathbf{v}. \quad (2.11)$$

As such, it is only the *total momentum* and the *total kinetic energy* of the gas, respectively

$$\sum_{p=1}^{P}\iint m_p\mathbf{v}f_p(t,\mathbf{x},\mathbf{v})\,\mathrm{d}\mathbf{x}\,\mathrm{d}\mathbf{v}, \text{ and } \sum_{p=1}^{P}\iint \frac{m_p}{2}|\mathbf{v}|^2 f_p(t,\mathbf{x},\mathbf{v})\,\mathrm{d}\mathbf{x}\,\mathrm{d}\mathbf{v},$$

that are conserved.

The H-theorem also applies to the multispecies case, for the *total Boltzmann entropy* and total dissipation:

$$\mathcal{H} = \sum_{p=1}^{P}\int f_p(\mathbf{v})\log(f_p(\mathbf{v}))\,\mathrm{d}\mathbf{v}, \quad \mathcal{S} = \sum_{p=1}^{P}\int \mathcal{Q}_p[f_p](\mathbf{v})\log(f_p(\mathbf{v}))\,\mathrm{d}\mathbf{v} \le 0,$$

see [17]. The equilibrium distributions are all Maxwellians with common average velocity, $\bar{\mathbf{v}}_{\text{eq}}$, and temperature, T_{eq}:

$$f_p = \mathcal{M}^{n,\bar{\mathbf{v}}_{\text{eq}},T_{\text{eq}}}(t,\mathbf{x},\mathbf{v}) = n_p(t,\mathbf{x})\left(\frac{m_p}{2\pi T_{\text{eq}}}\right)^{D_{\mathbf{v}}/2}\exp\left(-\frac{m_p(\bar{\mathbf{v}}_{\text{eq}}-\mathbf{v})^2}{2T_{\text{eq}}}\right). \tag{2.12}$$

Note n_p and the rest of individual moments are defined just as in Eq. (2.5):

$$n_p = \int f_p \,\mathrm{d}\mathbf{v}, \quad \rho_p\bar{\mathbf{v}}_p = \int m_p\mathbf{v}f_p \,\mathrm{d}\mathbf{v}, \quad \frac{D_{\mathbf{v}}}{2}n_pT_p = \int \frac{m_p}{2}(\bar{\mathbf{v}}_p-\mathbf{v})^2 f_p \,\mathrm{d}\mathbf{v},$$

where $\rho_p = m_p n_p$ and $\mathcal{P}_p = n_p T_p$. The total moments for the mixture are given by $n = \sum n_p$, $\rho = \sum \rho_p$, $\rho\bar{\mathbf{v}} = \sum \rho_p\bar{\mathbf{v}}_p$, $\mathcal{P} = \sum \mathcal{P}_p$, and

$$\frac{D_{\mathbf{v}}}{2}nT = \sum_{p=1}^{P}\int \frac{m_p}{2}(\bar{\mathbf{v}}-\mathbf{v})^2 f_p \,\mathrm{d}\mathbf{v}.$$

2.3 A Multispecies BGK Model

Although the multispecies Boltzmann equation described in Section 2.2 shares many features with the single species Boltzmann equation, the fact that conservations are only global in space and all species, e.g. (2.11), makes its simplification to a relaxation operator such as the BGK model (2.6) much harder. Many different approaches exists to derive such a multispecies BGK operator, but very few are satisfactory in regards to the macroscopic properties of the resulting relaxation operator. The interested reader can find more details about these various approaches in the recent papers [3, 11].

This work will follow along the lines of [31]. The formulation of the multispecies BGK operator requires the definition of the mixture Maxwellians:

$$\mathcal{M}_{p,q}[f_p,f_q](t,\mathbf{x},\mathbf{v}) = n_p(t,\mathbf{x})\left(\frac{m_p}{2\pi T_{p,q}}\right)^{D_{\mathbf{v}}/2}\exp\left(-\frac{m_p(\bar{\mathbf{v}}_{p,q}-\mathbf{v})^2}{2T_{p,q}}\right), \tag{2.13}$$

where $\bar{\mathbf{v}}_{p,q}$ and $T_{p,q}$ are mixture moments to be determined. It is assumed that the interaction of the p^{th} and the q^{th} species drives f_p towards $\mathcal{M}_{p,q}$, as well as f_q towards $\mathcal{M}_{q,p}$; thus we require $\bar{\mathbf{v}}_{p,q} = \bar{\mathbf{v}}_{q,p}$, $T_{p,q} = T_{q,p}$. Assuming the distributions are close to equilibrium permits the simplification of $\mathcal{Q}_{p,q}$ to obtain

$$\mathcal{Q}^{\text{BGK}}_{p,q}[f_p,f_q] = \nu_{p,q}(\mathcal{M}_{p,q}[f_p,f_q]-f_p), \tag{2.14}$$

where $\nu_{p,q}$ are positive collision rates to be determined. The multispecies BGK model is thus defined as the evolution law (2.7) together with the operator (2.14).

In order to recover the structural properties of the Boltzmann equation, the mixture moments have to be chosen appropriately. Considering the interaction of the p^{th} species with itself, we deduce $\bar{\mathbf{v}}_{p,p} = \bar{\mathbf{v}}_p$ and $T_{p,p} = T_p$. To define $\bar{\mathbf{v}}_{p,q}$, it is enough to impose the conservation of

momentum in the form of Eq. (2.10). This readily yields

$$\bar{\mathbf{v}}_{p,\,q} = \frac{\rho_p \nu_{p,\,q} \bar{\mathbf{v}}_p + \rho_q \nu_{q,\,p} \bar{\mathbf{v}}_q}{\rho_p \nu_{p,\,q} + \rho_q \nu_{q,\,p}}. \tag{2.15}$$

This expression is reminiscent to the microscopic parametrisation of the postcollisional velocities as a function of the precollisional ones (2.9). Similarly, requiring Eq. (2.11) as an expression of conservation of kinetic energy produces

$$T_{p,\,q} = \frac{n_p \nu_{p,\,q} T_p + n_q \nu_{q,\,p} T_q}{n_p \nu_{p,\,q} + n_q \nu_{q,\,p}} + \frac{\rho_p \nu_{p,\,q} (\bar{\mathbf{v}}_p^2 - \bar{\mathbf{v}}_{p,\,q}^2) + \rho_q \nu_{q,\,p} (\bar{\mathbf{v}}_q^2 - \bar{\mathbf{v}}_{q,\,p}^2)}{D_{\mathbf{v}} (n_p \nu_{p,\,q} + n_q \nu_{q,\,p})}. \tag{2.16}$$

This expression guarantees $T_{p,\,q} \geq 0$, see [31, Appendix 9]. These choices ensure, by construction, the conservation of total momentum and total kinetic energy of the gas.

This model also captures the dissipative structure of the multispecies Boltzmann equations. It is shown in [31] that the collision operator (2.14) verifies the H-theorem:

$$\mathcal{S} = \sum_{p=1}^{P} \int \mathcal{Q}_p^{\mathrm{BGK}}[f_p](\mathbf{v}) \log(f_p(\mathbf{v}))\, \mathrm{d}\mathbf{v} \leq 0.$$

2.4 Hydrodynamic Limits

We will briefly present here the zeroth order hydrodynamic limit of the multispecies BGK model (2.14), following along the lines of the recent paper [6]. Taking the limit $\varepsilon \to 0$ in that kinetic equation will formally project the distributions f_p towards the equilibrium distributions (2.12) whose moments solve a system of conservation laws. This system is obtained by multiplying the kinetic multispecies equation (2.7) by the powers of $\mathbf{v}$, integrating in velocity, and summing the equations on the individual moments in order to have only $D_{\mathbf{v}}$ equations for the total momentum.

Under the Maxwellian closure, we obtain the following system of $D_{\mathbf{v}} + P + 1$ conservation law, the so-called multispecies Euler limit of (2.7):

$$\begin{cases} \partial_t n_p + \nabla_{\mathbf{x}} \cdot (n_p \bar{\mathbf{v}}) = 0, \quad p \in \{1, \cdots, P\}, \\ \partial_t (\rho\, \bar{\mathbf{v}}) + \nabla_{\mathbf{x}} \cdot (\rho\, \bar{\mathbf{v}} \otimes \bar{\mathbf{v}}) + \nabla_{\mathbf{x}} (n\, T) = \mathbf{0}, \\ \partial_t \left(\frac{1}{2} \rho\, |\bar{\mathbf{v}}|^2 + \frac{D_{\mathbf{v}}}{2} n\, T \right) + \nabla_{\mathbf{x}} \cdot \left[\left(\frac{1}{2} \rho\, |\bar{\mathbf{v}}|^2 + \frac{D_{\mathbf{v}} + 2}{2} n\, T \right) \bar{\mathbf{v}} \right] = 0. \end{cases} \tag{2.17}$$

The interested reader can consult [6] for the terms corresponding to the next order in the expansion, the multispecies Navier-Stokes limit of (2.7).

3 Numerical Schemes

This section is devoted to the development of efficient numerical methods for the multispecies BGK model, given by Eqs. (2.7) and (2.14). The numerical simulation of the model is hindered by the presence of two radically different scales. The transport term classically imposes a CFL condition on the mesh size: $\Delta t \sim \mathcal{O}(\Delta x)$ is needed for stability. However, in the regimes

where $\varepsilon \ll 1$, the collision term dominates the dynamics, further restricting the time step to $\Delta t \sim \mathcal{O}(\varepsilon^{-1})$. This requirement is particularly pernicious in view of the large cost per step (due to the computation of non-local terms), and it would render a naïve scheme inefficient. The development of schemes for kinetic and hyperbolic equations which can handle multiple scales without such penalties (sometimes called *asymptotic-preserving* schemes) is a very active area of research, see the recent reviews [34, 23, 32].

In order to construct an efficient numerical scheme for Equation (2.7), we resort to *projective* and *telescopic projective integration*. First introduced in [29], projective integration provides an efficient framework for the numerical solution of differential equations with two distinct timescales, characterised by two separate clusters of eigenvalues. Telescopic projective integration was introduced by [30] in order to extend the method to problems with many scales, or without a clear spectral separation. These methods are not asymptotic preserving in the classical sense [33] because they cannot be evaluated at $\varepsilon = 0$ to recover a scheme for the asymptotic equation; nevertheless, they are able to solve stiff problems efficiently, and have been successfully adapted to some kinetic equations: radiative transfer [39], the linearised BGK equation with multiple relaxation times [47], and both the full BGK model and the Boltzmann equation [45, 46]. Higher-order approaches have also been developed [37, 38].

In the remainder of this section we describe the numerical method. First we introduce the phase space discretisation, using a discrete velocity method for the collision operator, coupled with a finite-volume scheme for the transport. Then we present the projective and telescopic schemes.

3.1 Phase Space Discretisation

Velocity The discretisation of Equation (2.7) can be conducted in a number of ways; see [23] for a survey. Here we shall employ a discrete velocity approach as in [51, 12, 48], where the velocity space is approximated by a finite grid. The choice of grid is non-trivial, and it can affect the entropic properties of the numerical scheme [1]; for simplicity, we choose a Cartesian grid.

The velocity space, $\mathbb{R}^{D_\mathbf{v}}$, is first restricted to a bounded domain $(-L_v, L_v)^{D_\mathbf{v}}$. Each dimension is discretised into $2N_v + 1$ points, separated by a distance $\Delta v = 2L_v/(2N_v + 1)$; the j^{th} point is given by $v_j = j\Delta v$, where $j \in \mathcal{N}_v \coloneqq \{-N_v, \cdots, N_v\}$. The discretised velocity space becomes $\mathcal{V} = \{\mathbf{v}_{\boldsymbol{j}} = (v_{j_1}, \cdots, v_{j_{D_\mathbf{v}}})\}$, where $\boldsymbol{j} = (j_1, \cdots, j_{D_\mathbf{v}}) \in \mathcal{N}_v^{D_\mathbf{v}}$ is a multi-index. Equation (2.7) thus becomes a system of transport equations:

$$\begin{cases} \partial_t f_{p,\boldsymbol{j}} + \mathbf{v}_{\boldsymbol{j}} \cdot \nabla_\mathbf{x} f_{p,\boldsymbol{j}} = \dfrac{1}{\varepsilon} \mathcal{Q}_{p,\boldsymbol{j}}[f_p], \quad \mathbf{x} \in \Omega \subseteq \mathbb{R}^{D_\mathbf{x}}, \, \boldsymbol{j} \in \mathcal{N}_v^{D_\mathbf{v}}, \, t > 0, \\ \mathcal{Q}_{p,\boldsymbol{j}}[f_p] = \displaystyle\sum_{q=1}^{P} \mathcal{Q}_{p,q,\boldsymbol{j}}[f_p, f_q], \end{cases} \tag{3.1}$$

where $f_{p,\boldsymbol{j}}$ approximates $f_p(\mathbf{v}_{\boldsymbol{j}})$, and $\mathcal{Q}_{p,q,\boldsymbol{j}}[f_p, f_q]$ approximates $\mathcal{Q}_{p,q}[f_p, f_q](\mathbf{v}_{\boldsymbol{j}})$. The initial datum $f_{p,\boldsymbol{j}}(0, \mathbf{x})$ is prescribed by evaluating the continuous datum, $f_{p,0}$, at $\mathbf{v}_{\boldsymbol{j}}$. Note that the evolution of $f_{p,\boldsymbol{j}}$ depends on $\mathcal{Q}_{p,\boldsymbol{j}}$, which itself depends on the entire distribution of every species, coupling all the equations in the system.

The evaluation of the collision operator will require the approximation of the moments of the distribution based on the discretised velocity grid. The semi-discrete individual moments are[3]

$$n_p^h = \sum f_{p,\boldsymbol{j}} \Delta \mathbf{v}, \quad \rho_p^h \bar{\mathbf{v}}_p^h = \sum m_p \mathbf{v}_{\boldsymbol{j}} f_{p,\boldsymbol{j}} \Delta v, \quad \frac{D_{\mathbf{v}}}{2} n_p^h T_p^h = \sum \frac{m_p}{2} (\bar{\mathbf{v}}_p^h - \mathbf{v}_{\boldsymbol{j}})^2 f_{p,\boldsymbol{j}} \Delta v, \tag{3.2}$$

where $\Delta \mathbf{v} = \Delta v^{D_{\mathbf{v}}}$, and $\rho_p^h = m_p n_p^h$ as before. The approximate mixture moments are computed as in Eqs. (2.15) and (2.16). The collision operator is, therefore,

$$\mathcal{Q}_{p,q,\boldsymbol{j}}^{\mathrm{BGK}}[f_p, f_q] = \nu_{p,q}(\mathcal{M}_{p,q,\boldsymbol{j}}[f_p, f_q] - f_{p,\boldsymbol{j}}), \tag{3.3}$$

where $\mathcal{M}_{p,q,\boldsymbol{j}}[f_p, f_q] = \mathcal{M}_{p,q}[f_p, f_q](\mathbf{v}_{\boldsymbol{j}})$, and $\mathcal{M}_{p,q}[f_p, f_q]$ is the Maxwellian (2.13) generated by the approximate moments.

Space The spatial discretisation of Equation (3.1) will be guided by the treatment of the transport term alone. Linear transport terms such as $\mathbf{v}_{\boldsymbol{j}} \cdot \nabla_{\mathbf{x}} f_{p,\boldsymbol{j}}$ can be discretised in a number of ways, including semi-Lagrangian methods [19, 18, 22] and finite-volume methods [41, 55, 42]. Here we shall prescribe a first-order finite-volume scheme, but this can be replaced with a higher-resolution method (a WENO scheme [43], for instance) independently of the choices for the discretisations of velocity and time.

The spatial domain, Ω, is assumed to be rectangular, of the form $(0, L_{x,1}) \times \cdots \times (0, L_{x,D_{\mathbf{x}}})$. Each dimension d is discretised into $N_{x,d}$ volumes of size $\Delta x_d = L_{x,d}/N_{x,d}$: every one, a cell $C_i = (x_{i-1/2}, x_{i+1/2})$ with centre x_i, where $x_i = i\Delta x$, for $i \in \mathcal{N}_x \coloneqq \{1, \cdots, N_x\}$. The discretised spatial domain becomes $\mathcal{X} = \{\boldsymbol{C}_{\boldsymbol{i}} = C_{i_1} \times \cdots \times C_{i_{D_{\mathbf{x}}}}\}$, where $\boldsymbol{i} = (i_1, \cdots, i_{D_{\mathbf{x}}}) \in \mathcal{N}_x^{D_{\mathbf{x}}}$ is a multi-index. Equation (3.1) thus becomes a system of equations:

$$\begin{cases} \partial_t f_{p,\boldsymbol{i},\boldsymbol{j}} + \Phi_{p,\boldsymbol{i},\boldsymbol{j}}[f_p] = \dfrac{1}{\varepsilon} \mathcal{Q}_{p,\boldsymbol{i},\boldsymbol{j}}[f_p], \quad \boldsymbol{i} \in \mathcal{N}_x^{D_{\mathbf{x}}}, \, \boldsymbol{j} \in \mathcal{N}_v^{D_{\mathbf{v}}}, \, t > 0, \\ \mathcal{Q}_{p,\boldsymbol{i},\boldsymbol{j}}[f_p] = \displaystyle\sum_{q=1}^{P} \mathcal{Q}_{p,q,\boldsymbol{i},\boldsymbol{j}}[f_p, f_q], \end{cases} \tag{3.4}$$

where $f_{p,\boldsymbol{i},\boldsymbol{j}}$ is a finite-volume approximation of $f_{p,\boldsymbol{j}}$, $f_{p,\boldsymbol{i},\boldsymbol{j}}(t) \simeq \frac{1}{|\boldsymbol{C}_{\boldsymbol{i}}|} \int_{\boldsymbol{C}_{\boldsymbol{i}}} f_{p,\boldsymbol{j}}(t, \mathbf{x}) \, \mathrm{d}\mathbf{x}$, with equality for the initial datum.

The term $\Phi_{p,\boldsymbol{i},\boldsymbol{j}}$, expresses the net flux across the boundary of $\boldsymbol{C}_{\boldsymbol{i}}$. In the one-dimensional setting, $D_{\mathbf{x}} = 1$, it is written in conservation form as

$$\Phi_{p,i,j}[f_p] = \frac{F_{p,i+1/2,j} - F_{p,i-1/2,j}}{\Delta x},$$

where

$$F_{p,i+1/2,j} = f_{p,i,j}(v_j)^+ + f_{p,i+1,j}(v_j)^-$$

[3] As with the integrals, the sums in this text are taken over the full velocity domain, unless otherwise stated:

$$\sum \Delta \mathbf{v} \equiv \sum_{\boldsymbol{j} \in \mathcal{N}_v^{D_{\mathbf{v}}}} \Delta \mathbf{v}.$$

is the upwind flux discretisation. The generalisation to higher dimensions is immediate, see [42], but the notation quickly becomes cumbersome.

The discretisation in space replaces the collision operator (3.3) with

$$\mathcal{Q}^{\mathrm{BGK}}_{p,\,q,\,\boldsymbol{i},\,\boldsymbol{j}}[f_p, f_q] = \nu_{p,\,q}(\mathcal{M}_{p,\,q,\,\boldsymbol{i},\,\boldsymbol{j}}[f_p, f_q] - f_{p,\,\boldsymbol{i},\,\boldsymbol{j}}),$$

where $\mathcal{M}_{p,\,q,\,\boldsymbol{i},\,\boldsymbol{j}}[f_p, f_q]$ is simply the Maxwellian computed from the discretisations of f_p, f_q in velocity and space. The moments given in (3.2) are easily discretised; for example,

$$n_p(t,\mathbf{x}) = \sum f_{p,\,\boldsymbol{j}}(t,\mathbf{x})\Delta\mathbf{v} \quad \text{becomes} \quad n_{p,\,\boldsymbol{i}}(t) = \sum f_{p,\,\boldsymbol{i},\,\boldsymbol{j}}(t)\Delta\mathbf{v}.$$

3.2 Projective Integration

Following the phase space discretisation, the multispecies BGK equation leads to the semi-discrete system (3.4). This can be summarised as

$$\partial_t f_{p,\,\boldsymbol{i},\,\boldsymbol{j}} = \mathcal{D}^{\varepsilon}[f_{p,\,\boldsymbol{i},\,\boldsymbol{j}}], \tag{3.5}$$

where p, $\boldsymbol{i}$, and $\boldsymbol{j}$ are, respectively, the species, spatial, and velocity indices, and where $\mathcal{D}^{\varepsilon}$ is an operator which comprises both discrete transport and collisions:

$$\mathcal{D}^{\varepsilon}[f_{p,\,\boldsymbol{i},\,\boldsymbol{j}}] \coloneqq -\Phi_{p,\,\boldsymbol{i},\,\boldsymbol{j}}[f_p] + \frac{1}{\varepsilon}\mathcal{Q}_{p,\,\boldsymbol{i},\,\boldsymbol{j}}[f_p].$$

Projective integration essentially consists of two stages: an inner step, where an elementary time-stepping method (the *inner integrator*) is used to solve (3.5) over a short interval; and a projective step, where the previous information is used to approximate the time derivative of f and extrapolate forward (through the *outer integrator*) over a large time interval.

We define step sizes Δt_0 and Δt_1, respectively for the inner and outer levels. The solution $f_{p,\,\boldsymbol{i},\,\boldsymbol{j}}(t)$ is approximated by $f^{n,\,k}_{p,\,\boldsymbol{i},\,\boldsymbol{j}}$ at the time $t = n\Delta t_1 + k\Delta t_0$. The evolution is computed as follows:

Inner Integrator The inner step is computed through the forward Euler method with step size Δt_0:

$$f^{n,\,k+1} = \mathrm{FE}_{\Delta t_0}[f^{n,\,k}] \coloneqq f^{n,\,k} + \Delta t_0 \mathcal{D}^{\varepsilon}[f^{n,\,k}], \tag{3.6}$$

where we have ommitted the p, $\boldsymbol{i}$, and $\boldsymbol{j}$ indices for simplicity. The inner step size will be chosen as $\Delta t_0 \sim \mathcal{O}(\varepsilon^{-1})$ to ensure the stability of (3.6), just as it would be in a classical scheme.

While higher-order inner integrators could easily be constructed, it is shown in [47] that forward Euler is the choice which gives the projective scheme the best stability properties. If high-order accuracy is desired, this can be achieved at the outer level.

Outer Integrator The outer step computes the update $f^{n+1,\,0}$ from $f^{n,\,0}$, which can be simply be understood as the steps f^{n+1} and f^n of a time discretisation $t = n\Delta t_1$. The outer step size will be chosen as $\Delta t_1 \sim \mathcal{O}(\Delta x)$.

In order to compute the update, the method first computes a sequence of $K+1$ inner updates from $f^{n,0}$, using the inner integrator. The last two updates, $f^{n,K}$ and $f^{n,K+1}$, are used to project the solution forward:

$$f^{n+1} = \mathrm{PFE}_{\Delta t_1}[f^n] := f^{n,K+1} + (\Delta t_1 - (K+1)\Delta t_0)\frac{f^{n,K+1} - f^{n,K}}{\Delta t_0}; \tag{3.7}$$

the relative size of the extrapolation is $M = \frac{\Delta t_1}{\Delta t_0} - (K+1)$.

Since the extrapolation is performed with a first-order approximation of the derivative, this is known as the *projective forward Euler method*. Higher order methods can be constructed by using more points to approximate the time derivative, in the vein of Runge-Kutta methods, as discussed in [29].

A schematic summary of the method can be found in Algorithm 1. The exact choice of K, Δt_0, and Δt_1 will be discussed in Section 4.

Algorithm 1: Projective Integration

```
Data: N, K, Δt_1, Δt_0
f^0 ← f(0) ;
for 0 ≤ n ≤ N − 1 do
    f^{n,0} ← f^n ;
    for 0 ≤ k ≤ K do
        f^{n,k+1} ← FE_{Δt_0}[f^{n,k}] ;
    end
    f^{n+1} ← PFE_{Δt_1}[f^n] ;
end
```

Efficiency of the Method As discussed in [30], the efficiency of projective integration can be measured by comparing the number of inner steps required to integrate over a time interval directly to that required by the projective method. Assuming a homogeneous cost per step and negligible overhead arising from the projection step (which is reasonable as the projective step does not involve the computation of moments of f), projective integration reduces the overall computational cost of a simulation by a factor of

$$S = \frac{\Delta t_1 (\Delta t_0)^{-1}}{K+1} = \frac{M+K+1}{K+1}.$$

3.3 Telescopic Integration

The stability properties of projective integration are well-understood: the method is suited for problems with exactly two timescales which are spectrally separate. There are, however, many multi-scale problems of interest whose spectra lack the sufficient structure: for instance, the linearised and the full BGK models, as soon as the collision rate ν depends on space or on the distribution f [47, 46, 36]. This is also the case for the multi-species BGK model (2.7, 2.14), as will be shown in Section 4.

Telescopic integration extends the projective method to include such problems. The method nests several levels: an innermost level, consisting, as before, of an elementary integrator; and

a number of outer levels, each performing a projection step based on the iterations of the level below it. We briefly discuss an approach with two projective levels, which will prove sufficient for our needs, though the method can easily be extended.

We define step sizes Δt_0, Δt_1, and Δt_2, respectively for the inner, middle, and outer levels. The solution $f_{p,\boldsymbol{i},\boldsymbol{j}}(t)$ is approximated by $f^{n,k,l}_{p,\boldsymbol{i},\boldsymbol{j}}$ at the time $t = n\Delta t_2 + k\Delta t_1 + l\Delta t_0$. The evolution is computed as follows:

The step of the outer integrator is given by

$$f^{n+1} = \mathrm{PFE}_{\Delta t_2}[f^n] \coloneqq f^{n,K_1+1} + (\Delta t_2 - (K_1+1)\Delta t_1)\frac{f^{n,K_1+1} - f^{n,K_1}}{\Delta t_1};$$

the relative size of the extrapolation is $M_1 = \frac{\Delta t_2}{\Delta t_1} - (K_1+1)$. In order to evaluate the update, K_1+1 steps of the middle integrator have to be performed, to find f^{n,K_1} and f^{n,K_1+1} from f^n. Each of those steps is given by

$$f^{n,k+1} = \mathrm{PFE}_{\Delta t_1}[f^{n,k}] \coloneqq f^{n,k,K_0+1} + (\Delta t_1 - (K_0+1)\Delta t_0)\frac{f^{n,k,K_0+1} - f^{n,k,K_0}}{\Delta t_0},$$

extrapolations of size $M_0 = \frac{\Delta t_1}{\Delta t_0} - (K_0+1)$. For each step to be performed, K_0+1 steps of the inner integrator have to be computed, to find f^{n,k,K_0} and f^{n,k,K_0+1} from $f^{n,k}$. These inner steps are, once again, given by the forward Euler method

$$f^{n,k,l+1} = \mathrm{FE}_{\Delta t_0}[f^{n,k,l}] \coloneqq f^{n,k,l} + \Delta t_0 \mathcal{D}^{\varepsilon}[f^{n,k,l}],$$

and can be computed directly. Since the outermost extrapolation is once again performed with a first-order approximation of the derivative, this is known as the (two-level) *telescopic projective forward Euler method*.

A schematic summary of the method is presented in Algorithm 1. Once again, the choice of parameters K_0, K_1, Δt_0, Δt_1, and Δt_2 will be discussed in Section 4.

Algorithm 2: Telescopic Integration (two levels)

```
Data: N, K_0, K_1, Δt_2, Δt_1, Δt_0
f^0 ← f(0) ;
for 0 ≤ n ≤ N − 1 do
    f^{n,0} ← f^n ;
    for 0 ≤ k ≤ K_0 do
        f^{n,k,0} ← f^{n,k} ;
        for 0 ≤ l ≤ K_1 do
            f^{n,k,l+1} ← FE_{Δt_0}[f^{n,k,l}] ;
        end
        f^{n,k+1} ← PFE_{Δt_1}[f^{n,k}] ;
    end
    f^{n+1} ← PFE_{Δt_2}[f^n] ;
end
```

Efficiency of the Method The efficiency of telescopic projective integration can be measured as in the previous section. The n^{th} level reduces the computational cost of a simulation by a factor of S_n, and the overall efficiency factor is S:

$$S_n = \frac{\Delta t_{n+1}(\Delta t_n)^{-1}}{K_n + 1} = \frac{M_n + K_n + 1}{K_n + 1}, \quad S = \prod_{n=1}^{N} S_n. \tag{3.8}$$

4 Spectra & Stability

The purpose of this section is to discuss the choice of integration parameters, Δt_i and K_i. We shall recall the stability analysis of [29, 30], and illustrate it in the context of kinetic equations, and the multispecies BGK model in particular.

The suitability of projective integration as a numerical method for kinetic equations with very small Knudsen numbers can be understood intuitively by considering their hydrodynamic asymptotics. As referenced in Section 2.4, Equations (2.1) and (2.7) can be studied in the limit $\varepsilon \to 0$, and their limiting behaviour can be characterised by systems of equations for the evolution of their moments. In the space of solutions, as the collision operator drives the state towards local equilibrium, trajectories rapidly arrive at a hypersurface comprised only of Maxwellian distributions, see Fig. 1 for a diagram. Once on this surface, the only possible evolution is within, which corresponds to the evolution of the distribution's moments as governed by the corresponding macroscopic system. For small values of ε, the arrival to and the evolution within the Maxwellian surface occur in very different time scales.

As discussed in Section 3, resolving both of these time scales with a typical scheme proves very costly, since a typical integrator will require steps of size $\Delta t \sim \mathcal{O}(\varepsilon^{-1})$ for stability. However, the two-scale nature of the problem can be exploited to escape this restriction: the integrator is permitted large steps (whose size are limited only by a hyperbolic CFL-like condition), as long as they alternate with smaller steps which ensure the return to the equilibrium hypersurface, as sketched in Fig. 2.

This intuitive portrayal can be formalised by performing error stability analysis on the projective integration and telescopic integration methods. An asymptotic stability result is presented in [29]: for large M, the stability region for the projective Euler method approaches two disjoint disks on the $\Delta t_0 \lambda$ complex plane; $\mathcal{D}\left(-1, M^{-1/K}\right)$ and $\mathcal{D}\left(-M^{-1}, M^{-1}\right)$, where by $\mathcal{D}(c, r)$ we

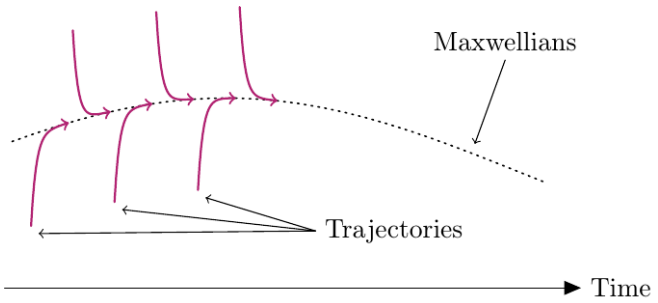

Figure 1: Trajectories in solution space for systems with Knudsen number in the hydrodynamic regime.

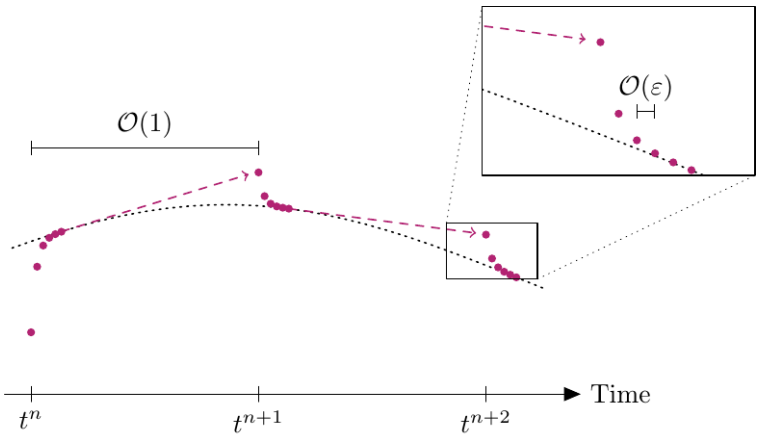

Figure 2: Sketch of projective integration: the method performs steps of size $\mathcal{O}(1)$, but introduces intermediate steps of size $\mathcal{O}(\varepsilon)$ to ensure the overall stability of the numerical solution.

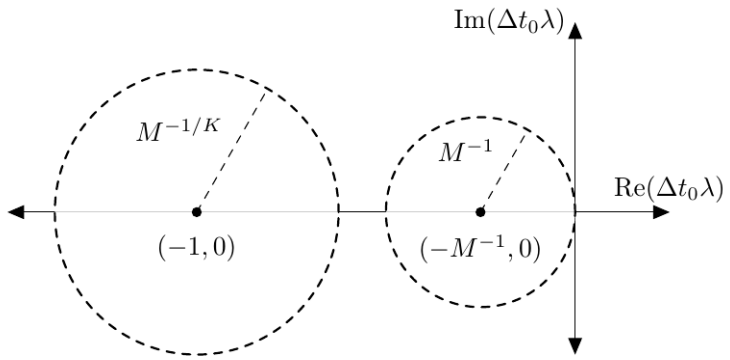

Figure 3: Asymptotic stability region for the projective forward Euler integrator.

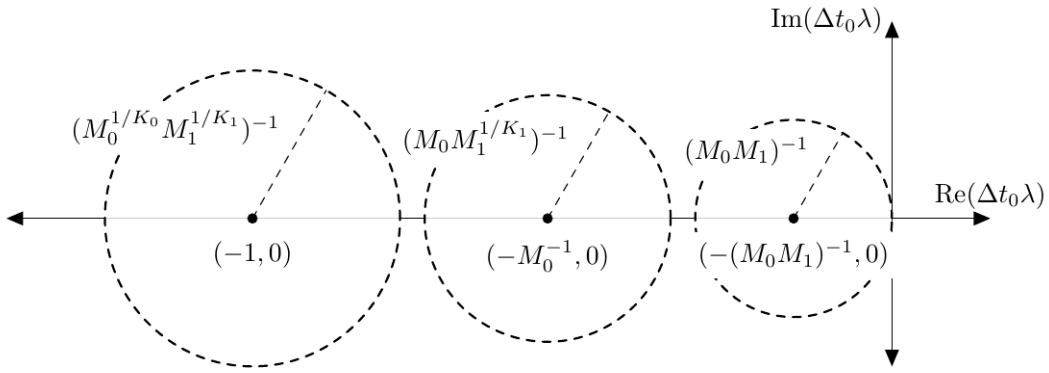

Figure 4: Asymptotic stability region for the telescopic projective forward Euler integrator.

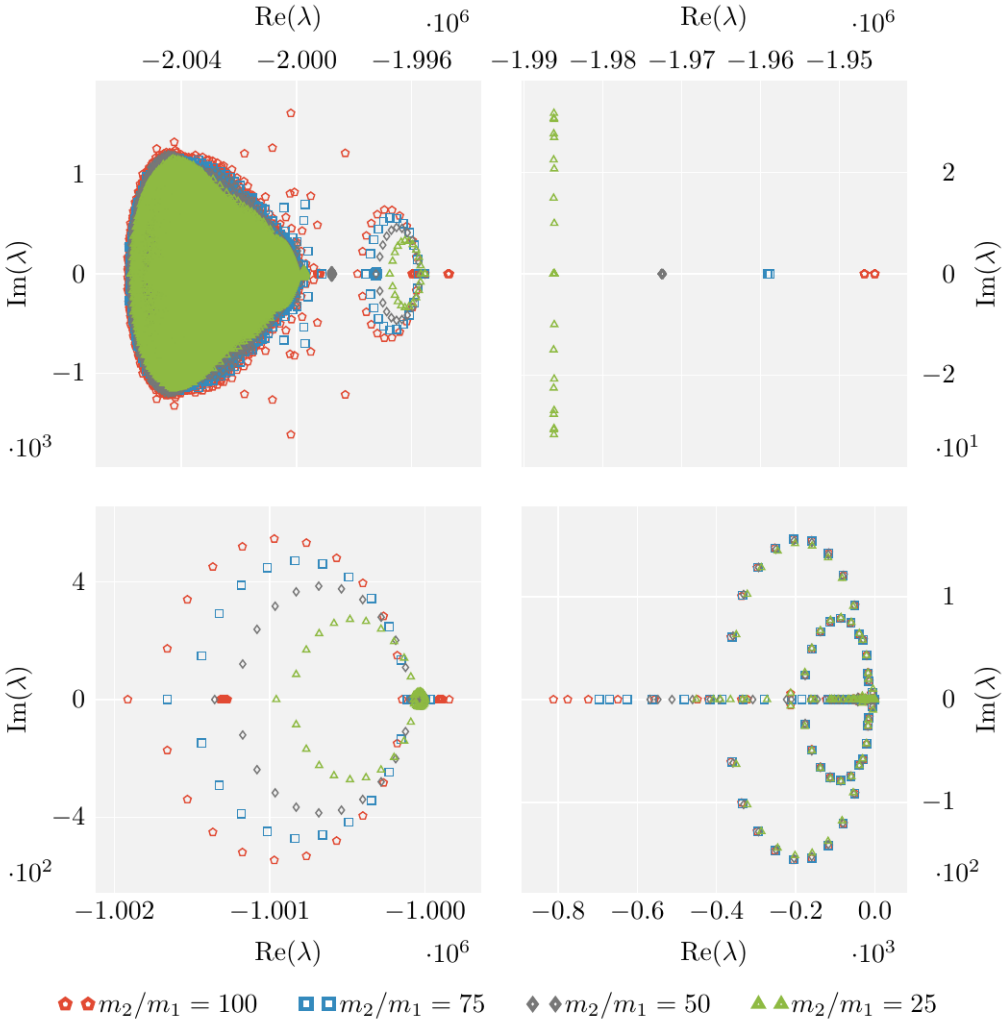

Figure 5: Approximate spectra for mixture Sod Tube problem of Section 5.1: various mass ratios. **Top**: fast modes, $\mathcal{O}(\varepsilon)$ (split across two regions). **Bottom left**: middle modes. **Bottom right**: slow modes, $\mathcal{O}(1)$.

mean the disk centred at the complex number c with radius r (see Fig. 3). The two-disk stability region is perfectly suited for a two-cluster spectrum, which often lies behind the fast-slow dynamics described above. Once the spectrum is known, the parameters Δt_0, K, and M can be chosen so that the scaled eigenmodes, $\Delta t_0 \lambda$, lie within the two stable disks: the fast modes will be contained in the left disk, and the slow modes, in the right disk. As a curiosity, note that the right disk corresponds to the stability region of a standard forward Euler method with step $\Delta t_0 M$; this is indeed the step size of the projection (3.7).

In more complex settings, a two-disk stability region might not suffice. For instance, the BGK model with a density-dependent collision frequency, the full Boltzmann equation, and the multispecies BGK model which we consider in this work all lead to more complicated spectra. Fortunately, telescopic projective methods also lead to richer stability regions, and can be used for our purposes. In the same vein as [29], we find that the two-level telescopic projective Euler method comprises three disks when M_0 and M_1 are large: $\mathcal{D}\left(-1, M_0^{-1/K_0} M_1^{-1/K_1}\right)$, $\mathcal{D}\left(-M_0^{-1}, M_0^{-1} M_1^{-1/K_1}\right)$, and $\mathcal{D}\left(-M_0^{-1} M_1^{-1}, M_0^{-1} M_1^{-1}\right)$ (see Fig. 4). As before, the parameters Δt_0, K_0, K_1, M_0, and M_1 have to be chosen so that the scaled eigenmodes lie within the stability region. This three-disk configuration is featured in the spectra of the numerical experiments discussed in Sections 5.2 to 5.4.

4.1 Estimating Spectra

The parameter choice strategy presented above relies entirely on accurate spectral information for the problems in question. However, finding the spectrum of kinetic equations, or even establishing partial information (such as bounds, number of clusters, or spectral gaps) is a difficult problem. For the single species Boltzmann equation, we refer to the classic paper of [24], or to its L^1 extension [49]. The multispecies theory is sparse, though we highlight the recent works [10, 20].

Our approach in this work will be to estimate the spectra of the problems numerically. We will consider the semi-discrete problem (3.5), evaluate the Jacobian of the operator $\mathcal{D}^\varepsilon$ through finite differencing, and compute the eigenvalues of the resulting matrix as an approximate spectrum for the problem. This approach proves extremely successful, as it permits finding optimal integration parameters for all of the numerical experiments of Section 5. Furthermore, exploiting the mild dependence of the spectra in the dimension of the problem [24], we are able to use the spectra of one-dimensional problems in order to find suitable parameters for problems in higher dimensions.

We present in Fig. 5 the spectra used in the mixture Sod Tube problem of Section 5.1 for mass ratios ranging from $m_1/m_2 = 25$ to $m_1/m_2 = 100$. The slow modes and middle modes, shown in the bottom right and bottom left plots respectively, are seen not to vary significantly across the different ratios, and therefore have similar stability properties.

However, this is not the case for the fastest modes. The fast cluster is shown across two plot panels in Fig. 5: the top left panel comprises the majority of fast modes, which vary slightly; the top right panel shows the rightmost fast modes, which vary greatly as the mass ratio increases. Across the different ratios, the width of the fast cluster grows by an order of magnitude. This spreading of the fast cluster, and the associated reduction in the gap, is consistent with the results in [10].

In practice, the widening of the cluster leads to different stability requirements: in the corresponding numerical test, the parameters used in the $m_1/m_2 = 1$ case also work for the

$m_1/m_2 = 100$ case, with the exception of K_1; the step number of the second level is increased from 6 to 14. This logarithmic scaling of the computational cost with the stiffness of the problem has been reported in [45] in the single-species setting.

5 Numerical Experiments

In this section, we apply our schemes to various physical scenarios in order to showcase the robustness and versatility of the methods. We will consider one example with $D_{\mathbf{x}} = D_{\mathbf{v}} = 1$, the mixture Sod Tube, and three examples with $D_{\mathbf{x}} = D_{\mathbf{v}} = 2$: a shock-bubble interaction, a Kelvin-Helmholtz instability, and a Richtmyer-Meshkov instability. The examples demonstrate the ability of the schemes to deal with complex scenarios, as well as their superior efficiency.

5.1 Mixture Sod Tube & Extreme Mass Ratios (1D / 1D)

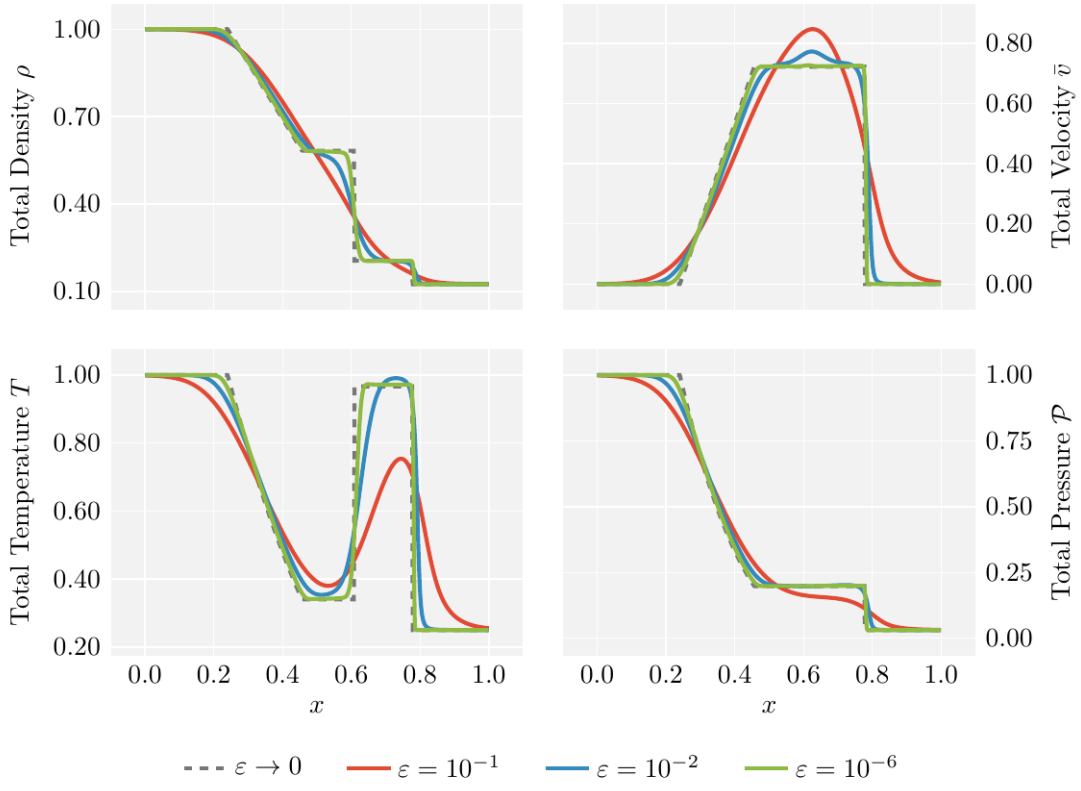

Figure 6: Mixture Sod Tube problem: numerical solutions with decreasing Knudsen number and unit mass ratio. The solutions approach the correct $\varepsilon \to 0$ limit.

Our first experiment is a generalisation of the Sod Tube problem [53]. The Sod Tube is a generic Riemann problem for the Euler system (2.17) (with a single species). A discontinuous initial datum is prescribed, which immediately develops a range of hyperbolic phenomena: a rar-

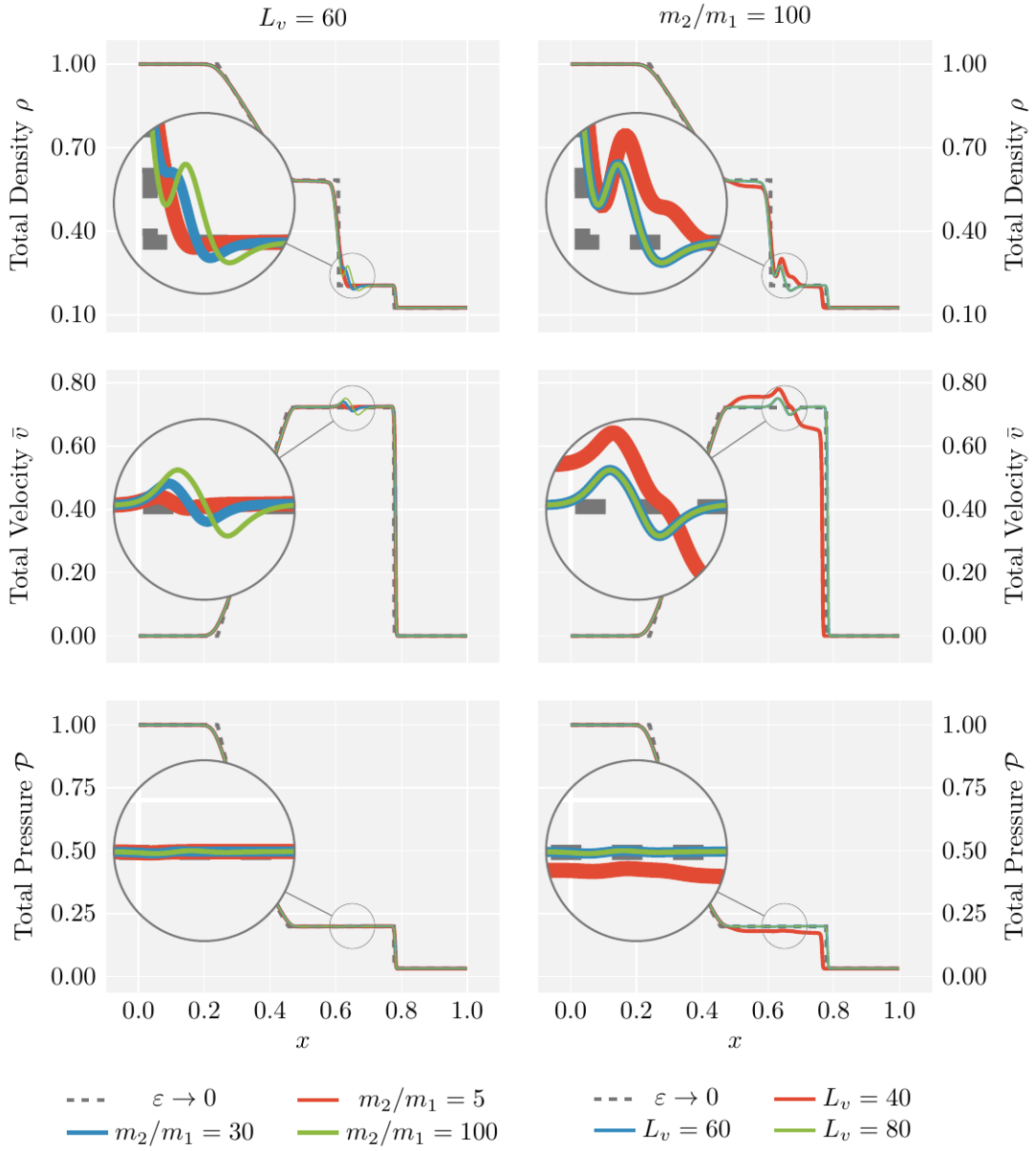

Figure 7: Mixture Sod Tube problem: extreme mass ratios. **Left**: higher mass ratios yield slower hydrodynamic convergence. **Right**: high mass ratios require larger velocity domains $(-L_v, L_v)$ in order to capture the correct behaviour.

efaction wave, a shock wave, and a contact discontinuity. Nevertheless, the solution is analytically tractable, yielding an ideal test case for numerical schemes.

We shall employ here a setting twice removed from the classical Sod Tube. Firstly, we entertain an analogue of the Riemann problem which involves two initially separate gases, whose solution can be constructed in the same fashion as that of the classical problem; see the appendix for the derivation. Secondly, rather than solving a multifluid Euler system, we solve the corresponding problem for the multispecies BGK model, and compare its moments to the aforementioned analytic solution, exploiting the limiting behaviour discussed in Section 2.4.

We will consider two gases in a one-dimensional domain $\Omega = (0, 1)$. The mass ratio m_2/m_1 and Knudsen number will vary through the examples. The initial configuration will emulate a Riemann problem with left state $(\rho_L, v_L, \mathcal{P}_L) = (1, 0, 1)$ and right state $(\rho_R, v_R, \mathcal{P}_R) = (2^{-3}, 0, 2^{-5})$, where the left state is entirely comprised of the first gas, and the right state of the second. To that end, we prescribe their initial distributions as Maxwellians with moments

$$\begin{cases} \rho_1 = (1-\delta)\rho_L, & \rho_2 = \delta\rho_L, & \bar{v}_1 = \bar{v}_2 = v_L, & \mathcal{P}_1 = \mathcal{P}_2 = \mathcal{P}_L, & \text{if } x \leq 0.5; \\ \rho_1 = \delta\rho_R, & \rho_2 = (1-\delta)\rho_R, & \bar{v}_1 = \bar{v}_2 = v_R, & \mathcal{P}_1 = \mathcal{P}_2 = \mathcal{P}_R, & \text{if } x > 0.5. \end{cases} \tag{5.1}$$

Ideally, we would set $\delta = 0$, but this leads to an ill-defined temperature, so we let $\delta = 10^{-5}$. This pattern will also be used in later experiments whenever a density is zero. We henceforth refer to this problem as the *mixture Sod Tube problem*.

To begin, we verify the behaviour of this problem in the hydrodynamic limit. We will compute numerically the solution with datum Eq. (5.1) with mass ratio $m_2/m_1 = 1$, for three different values of the Knudsen number: $\varepsilon = 10^{-1}$, 10^{-2}, and 10^{-6}. The larger values of epsilon do not pose significant stiffness, so a direct integration method can be used; for $\varepsilon = 10^{-6}$, we resort to a telescopic two-level method.

The solution is computed over the time interval $t \in (0, 0.15)$. The domain Ω is discretised with $\Delta x = 2^{-10}$, and the velocity space is set as $(-20, 20)$, with $\Delta v = 2^{-4}$. For the direct method employed on the larger values of ε, we let $\Delta t = 1.53 \times 10^{-5}$. In the telescopic method, we choose $\Delta t_0 = 5 \times 10^{-7}$, $\Delta t_1 = 2 \times 10^{-6}$, and $\Delta t_2 = 6.1 \times 10^{-5}$, and step numbers $K_0 = 1$ and $K_1 = 6$. We impose no-flux boundary conditions.

Figure 6 shows the numerical solutions superimposed on the analytical limiting solution (computed through the procedure detailed in the appendix). As the Knudsen number decreases, the moments of the solution approach the correct hydrodynamic limit.

It is of great interest to attempt the numerical solution of problems with extremely large mass ratios. Indeed, a simple mixture of Ar and He exhibits a mass ratio of 10, which can be a problem for some numerical methods, as noted in [59]. Their method can deal with mass ratios up to 35; however, ratios twice as large can easily be found in other scenarios, such as mixtures of H_2 and Xe.

We will demonstrate the behaviour of our scheme in the context of a hydrodynamic limit under an extreme mass ratio. Conveniently, the asymptotic behaviour of the mixture Sod Tube problem remains unchanged if we assume that the gases have different molecular masses; therefore, it remains a suitable validation case.

We solve the problem for mass ratios $m_2/m_1 = 5$, 30, and 100, in the hydrodynamic regime and compare the solutions. We let $\varepsilon = 10^{-6}$. The spatial discretisation is done as before. The velocity space is set as $(-60, 60)$, with $\Delta v = 2^{-4}$; such large domain is unnecessary for the

Physical		Phase space discretisation			Time discretisation		
m_1	1	Δx	2.5×10^{-2}		K_0	1	
m_2	5	Δy	2.5×10^{-2}	$(= \Delta x)$	K_1	6	
ε	10^{-5}	Δv	2.5×10^{-1}		Δt_0	5×10^{-6}	$(= \varepsilon/2)$
					Δt_1	2×10^{-5}	$(= 2\varepsilon)$
					Δt_2	1.25×10^{-3}	$(= \Delta x/20)$

Table 1: Parameters for the shock-bubble interaction test of Section 5.2, see Figs. 8 to 10

smaller mass ratios, but will be required for $m_2/m_1 = 100$. We again choose $\Delta t_0 = 5 \times 10^{-7}$, $\Delta t_1 = 2 \times 10^{-6}$, and $\Delta t_2 = 6.1 \times 10^{-5}$, though this time we set $K_0 = 1$ and $K_1 = 14$; again, the large step number is only required for the larger mass ratios. In order to justify our velocity discretisation, we will also solve the $m_2/m_1 = 100$ case with varying velocity spaces $(-L_v, L_v)$, for $L_v = 40$, 60, and 80, keeping the rest of the parameters fixed.

In all cases we deal with the large velocity supports directly. The recent work [11] has used a rescaling velocity approach reminiscent of [26] to overcome the same issue, but their strategy remains limited to mass ratios up to 20.

Figure 7 shows the numerical solutions, again superimposed on the limiting solution. The effects of the extreme mass ratios can be seen at point of contact discontinuity (the boundary between the two gases), magnified in the figure. The left column shows the solutions with various mass ratios; the overall hydrodynamic limit is captured well. However, the interfacial effects are more pronounced as the mass ratio increases, and will require a smaller Knudsen number before they become imperceptible. The right column shows the effect of the choice of velocity domain in the solution: $L_v = 40$ leads to widespread error, whereas $L_v = 60$ recovers the correct behaviour, and is in fact indistinguishable from $L_v = 80$.

5.2 Shock-Bubble Interaction (2D / 2D)

We investigate the interaction between a travelling shock and a smooth stationary bubble. This is a multispecies adaptation of a one-species test case proposed in [56]; the original test has been used to validate numerical schemes for the BGK model [13], including projective integration [46].

We will consider a mixture of two gases with mass ratio $m_2/m_1 = 5$ in a rectangular domain $\Omega = (-1.5, 3) \times (-1.5, 1.5)$. The Knudsen number is chosen in the hydrodynamic regime, $\varepsilon = 10^{-5}$. The initial configuration of the first (lighter) gas is a normal shock wave of Mach number $\mathrm{Ma} = 2$ propagating in the positive x-direction. Its initial distribution, $f_1(0, \mathbf{x}, \mathbf{v})$, is chosen as the Maxwellian corresponding to the following Riemann datum:

$$\begin{cases} \rho_1 = 2, & \bar{v}_{1,x} = 1.414, & \bar{v}_{1,y} = 0, & T_1 = 2.5, & \text{if } x \leq -1; \\ \rho_1 = 1, & \bar{v}_{1,x} = 0, & \bar{v}_{1,y} = 0, & T_1 = 1, & \text{if } x > -1. \end{cases} \tag{5.2}$$

The second (heavier) gas is initially stationary: a Maxwellian with density

$$\rho_2(0, \mathbf{x}) = \exp\Big\{-16|\mathbf{x} - \mathbf{x}_0|^2\Big\}. \tag{5.3}$$

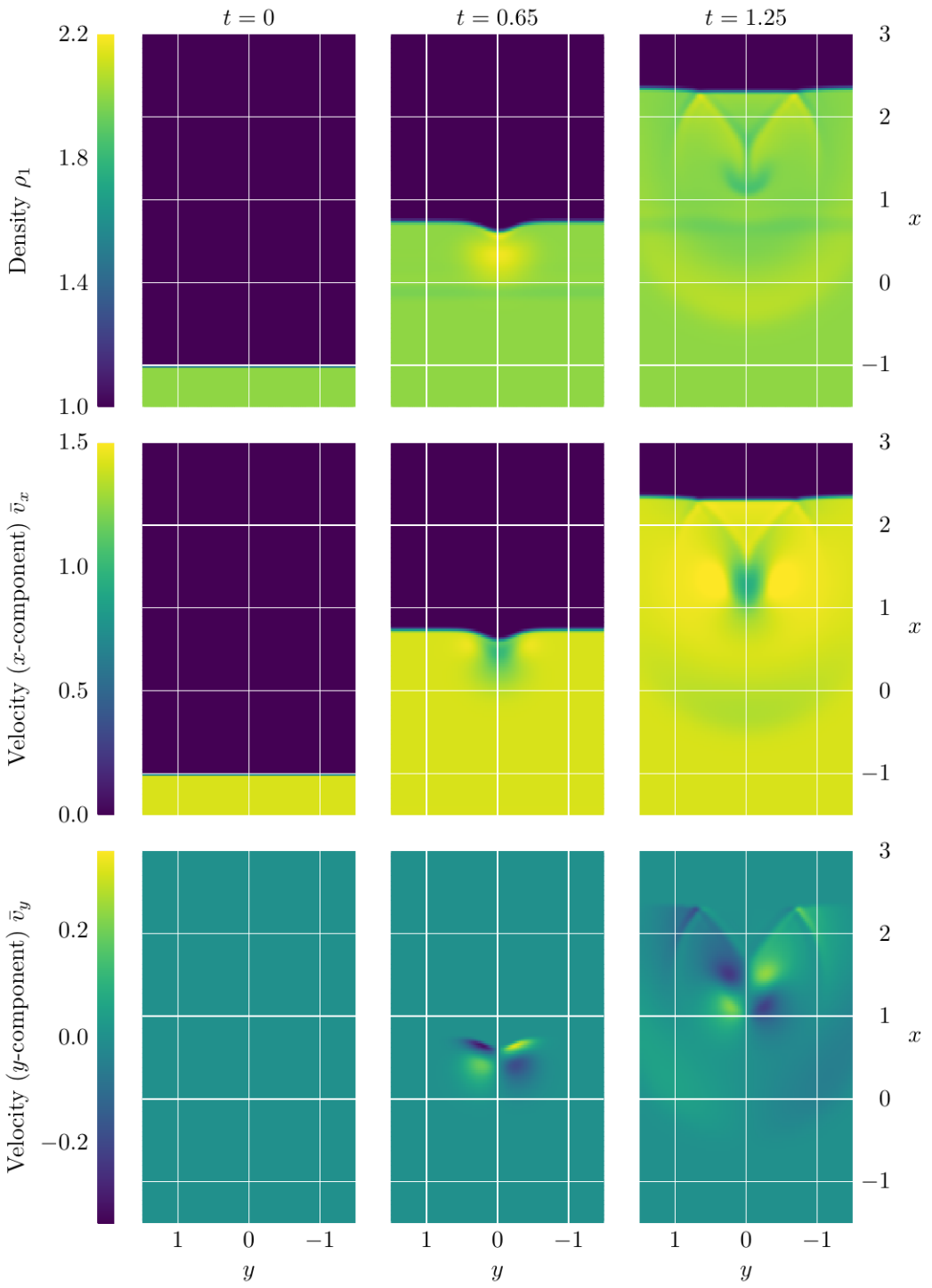

Figure 8: Shock-bubble interaction: evolution of the first (lighter) species. **Left**: datum. **Middle**: shock interacts with bubble. **Right**: pressure waves arise as a result of the shock-bubble interaction. Simulation parameters can be found in Table 1.

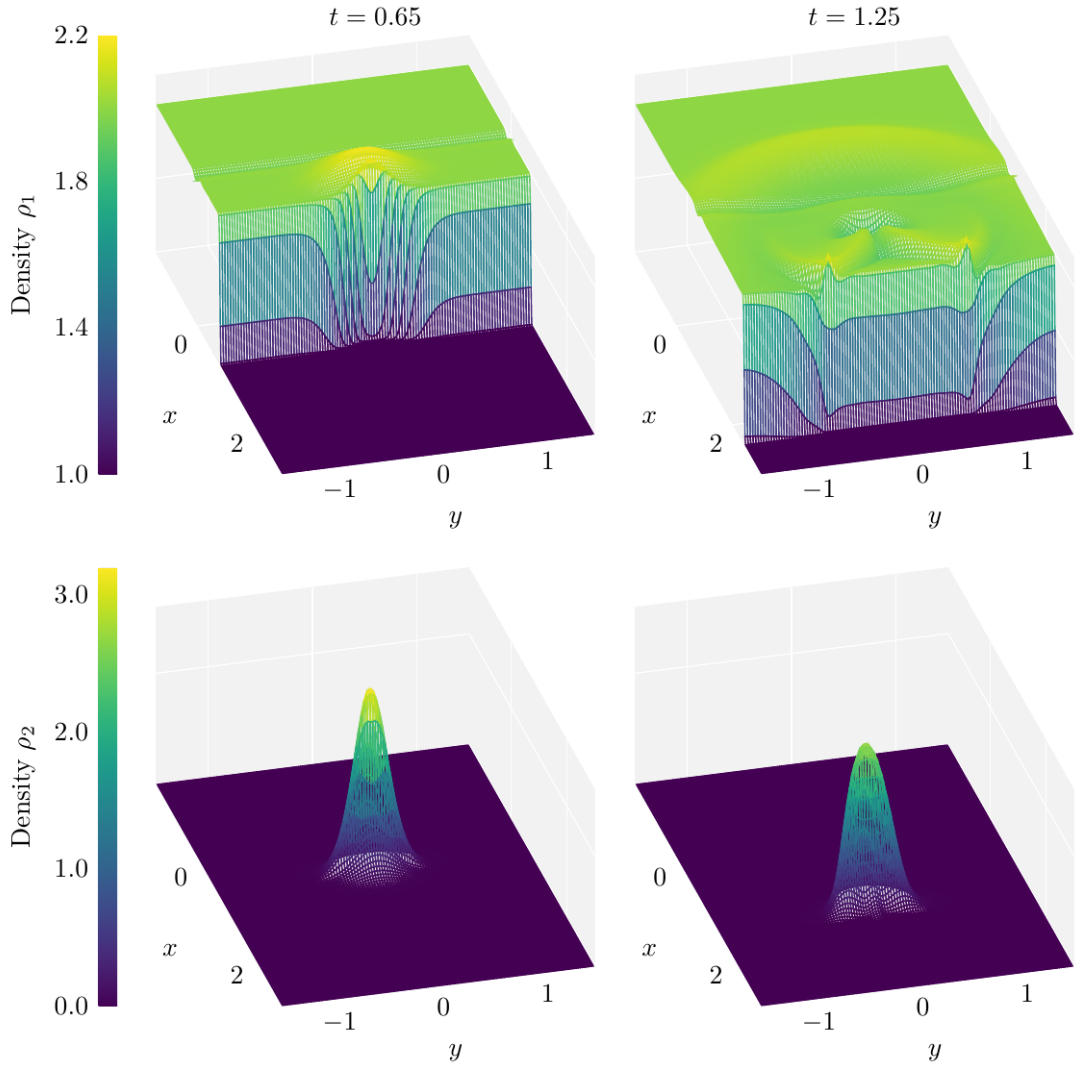

Figure 9: Shock-bubble interaction: evolution of the densities. **Left**: shock interacts with bubble. **Right**: bubble is dragged and deformed by the stream. Simulation parameters can be found in Table 1.

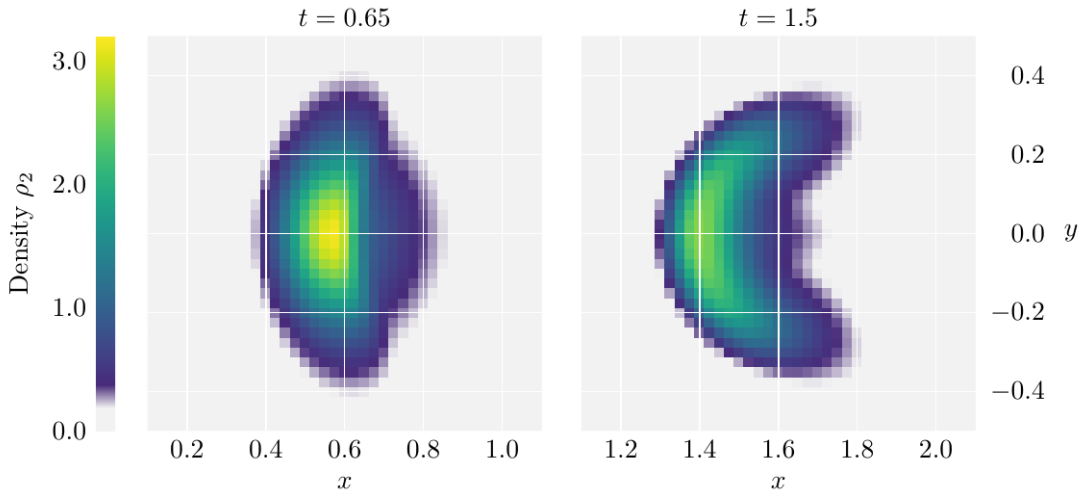

Figure 10: Shock-bubble interaction: detail of the bubble (second species). **Left**: the bubble has been compressed by the shock. **Right**: the bubble is displaced by the stream and deforms into a "C shape". Simulation parameters can be found in Table 1.

The temperatures of both gases around the bubble are chosen equal to each other and in such a way that there is unit total pressure:

$$T_1(0, \mathbf{x}) = T_2(0, \mathbf{x}) = (n_1(0, \mathbf{x}) + n_2(0, \mathbf{x}))^{-1}, \tag{5.4}$$

which is consistent with the right state in Eq. (5.2).

Numerically, the domain Ω is discretised with $\Delta x = \Delta y = 2.5 \times 10^{-2}$ (180×120 cells). The velocity space is set as $(-12, 12)^2$, with $\Delta v = 2.5 \times 10^{-1}$ (96^2 cells). In total, the phase space is discretised with 199,065,600 cells. We impose outflow boundary conditions.

The solution corresponding to Eqs. (5.2) to (5.4) is computed over the time $t \in (0, 1.5)$. We employ the telescopic two-level method, with step sizes $\Delta t_0 = 5 \times 10^{-6}$, $\Delta t_1 = 2 \times 10^{-5}$, and $\Delta t_2 = 1.25 \times 10^{-3}$, and step numbers $K_0 = 1$ and $K_1 = 6$. The inner steps follow the pattern $4\Delta t_0 = 2\varepsilon = \Delta t_1$. The outermost step is restricted by the stability of the transport scheme, rather than the projective integration. The use of telescopic projective integration decreases the computational cost by a factor of $S \simeq 18$, as defined in Eq. (3.8). This factor, considering the fine and high-dimensional mesh employed here, is extremely beneficial, reducing the simulation time from a matter of days to a matter of hours!

Figure 8 shows the evolution of the first (lighter) gas at several times. The shock travels to meet the bubble; when they meet, the central ($y \simeq 0$) portion of the shock is slowed down. As the shock traverses the bubble, two pressure waves are formed: one travelling upstream, appears as a reflection from the initial shock-bubble interaction; the second, travelling downstream, arises as the shock surrounds the obstacle and both "arms" meet behind the bubble.

Figure 9 compares the densities of either gas, and Fig. 10 presents a detailed view of the bubble. The bubble is compressed by the shock when it first arrives. As the shock passes, the bubble is displaced downstream and deforms into a "C shape".

A summary of the simulation parameters can be found in Table 1.

Physical		Phase space discretisation			Time discretisation		
m_1	1	Δx	7.8125×10^{-3}	$(= 2^{-7})$	K_0	2	
m_2	5	Δy	7.8125×10^{-3}	$(= \Delta x)$	K_1	4	
ε	10^{-5}	Δv	5×10^{-1}		Δt_0	5×10^{-6}	$(= \varepsilon/2)$
					Δt_1	2×10^{-5}	$(= 2\varepsilon)$
					Δt_2	$3.906\,25 \times 10^{-4}$	$(= \Delta x/20)$

Table 2: Parameters for the Kelvin-Helmholtz instability test of Section 5.3.

5.3 Kelvin-Helmholtz Instability (2D / 2D)

We turn our attention to the Kelvin-Helmholtz instability. This is a well-known phenomenon where vortices arise at the interface of two fluids with different density moving at different speeds. This test was also used to validate projective integration for the single-species BGK model in [46], with an initial configuration drawn from [44]. Here we shall present a two-species analogue.

We consider two gases with mass ratio $m_2/m_1 = 5$ in a square domain $\Omega = (-0.5, 0.5)^2$, periodic along the x-direction. The Knudsen number is chosen in the hydrodynamic regime, $\varepsilon = 10^{-5}$; higher values do not yield sufficiently defined vortices. The gases are initially separate: the first (lighter) gas occupies the $y \geq 0$ region, with density $\rho_1 = 1$ and horizontal velocity $\bar{v}_{1,x} = 0.5$; the second (heavier) gas occupies the $y < 0$ region, with density $\rho_2 = 2$ and horizontal velocity $\bar{v}_{2,x} = -0.5$. Their temperatures are chosen to ensure there is equal unit pressure across the boundary: $T_1 = n_1^{-1}$, $T_2 = n_2^{-1}$. Both gases are given a small vertical velocity to induce vorticity: $\bar{v}_{1,y} = \bar{v}_{2,y} = 10^{-2}\sin(4\pi x)$. The initial distribution of the gases are the Maxwellians corresponding to these moments.

Numerically, the domain Ω is discretised with $\Delta x = \Delta y = 7.8125 \times 10^{-3}$ (128^2 cells). The velocity space is set as $(-8, 8)^2$, with $\Delta v = 5 \times 10^{-1}$ (32^2 cells). In total, the phase space is discretised with 16,777,216 cells. We impose outflow boundary conditions along the non-periodic boundaries.

The solution is computed over the time $t \in (0, 3)$. We employ the telescopic two-level method, with step sizes $\Delta t_0 = 5 \times 10^{-6}$, $\Delta t_1 = 2 \times 10^{-5}$, and $\Delta t_2 = 3.906\,25 \times 10^{-4}$, and inner steps $K_0 = 2$ and $K_1 = 4$. Again the inner steps follow the pattern $4\Delta t_0 = 2\varepsilon = \Delta t_1$, and the outermost step is restricted by the hyperbolic CFL condition. The use of telescopic projective integration decreases the computational cost by a factor of $S \simeq 5$, as defined in Eq. (3.8).

Figure 11 shows the evolution of the densities of each gas as well as the total pressure. The small initial vertical perturbation results in the undulation of the interface. The relative difference in horizontal velocity rapidly causes the formation of clearly defined vortices. As the shear stress, the vortices are smeared horizontally.

Figure 12 studies the vortex structure at the time corresponding to the middle column of Fig. 11, where vorticity is at a peak. The figure displays the modulus of the total velocity $\bar{\mathbf{v}}$; the streamlines are superimposed.

A summary of the simulation parameters can be found in Table 2.

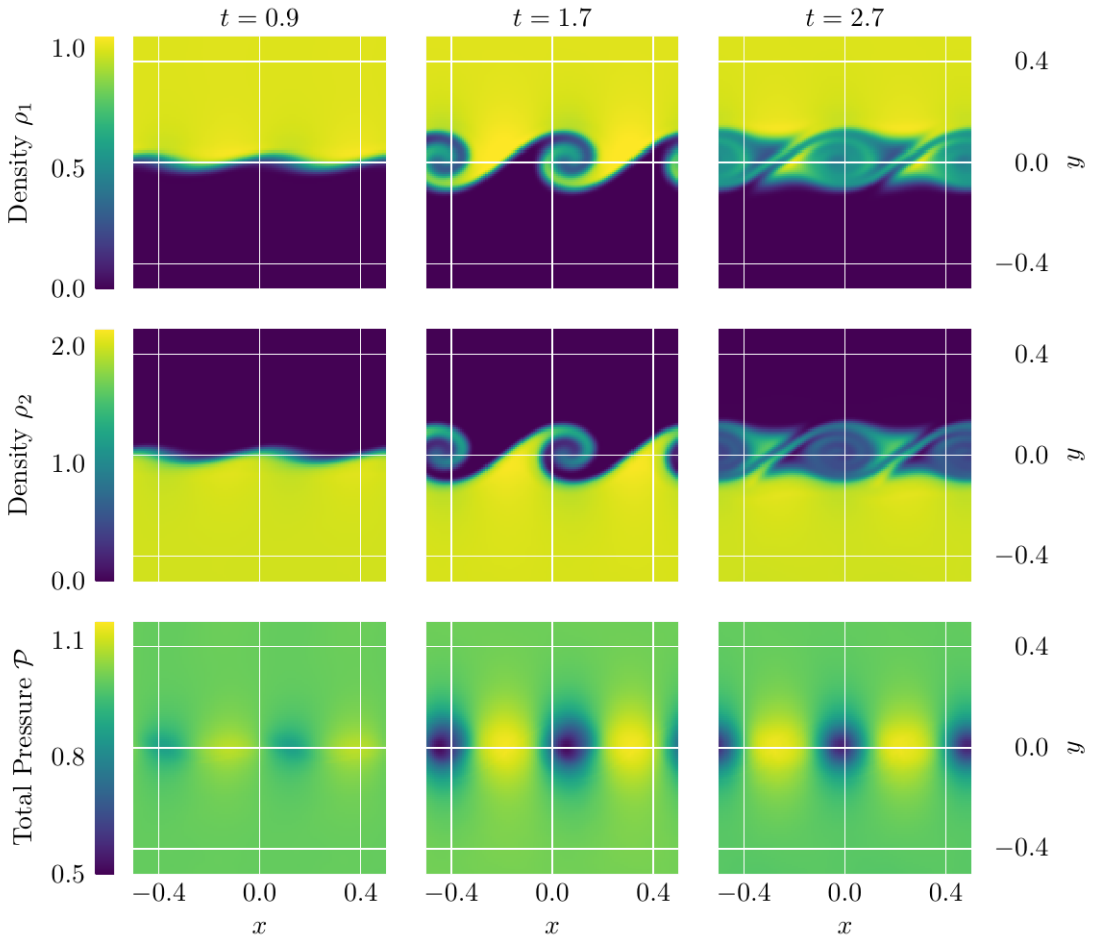

Figure 11: Kelvin-Helmholtz instability: evolution in time. **Left**: undulations appear on the gas interface. **Middle**: clear vortices have developed. **Right**: vortices begin to smear and merge. Simulation parameters can be found in Table 2.

Physical		Phase space discretisation			Time discretisation		
m_1	1	Δx	2.5×10^{-4}		K_0	1	
m_2	5	Δy	2.5×10^{-4}	$(= \Delta x)$	K_1	6	
ε	10^{-6}	Δv	2.5×10^{-1}		Δt_0	5×10^{-7}	$(= \varepsilon/2)$
					Δt_1	2×10^{-6}	$(= 2\varepsilon)$
					Δt_2	6.25×10^{-5}	$(= \Delta x/4)$

Table 3: Parameters for the Richtmyer-Meshkov instability test of Section 5.4.

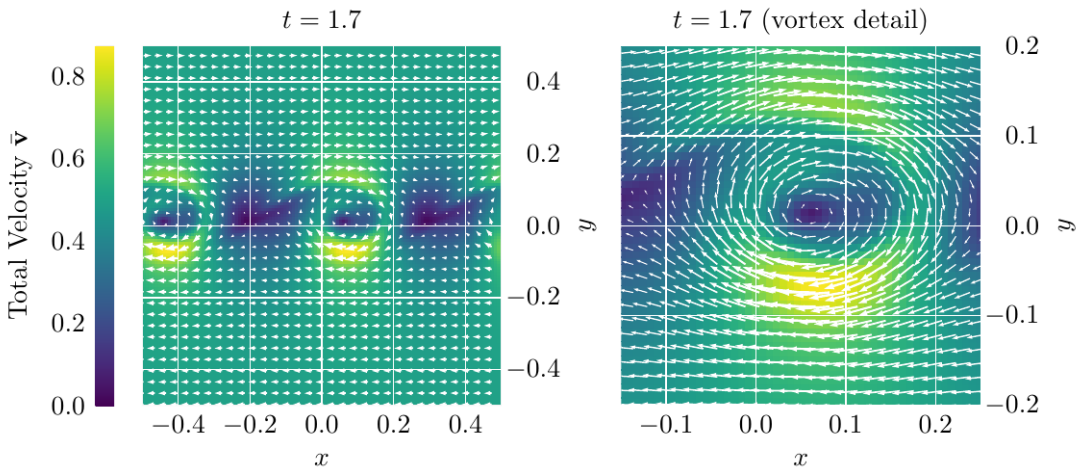

Figure 12: Kelvin-Helmholtz instability: modulus of the total velocity $\bar{\mathbf{v}}$ and stream lines at peak vorticity. **Left**: whole domain. **Right**: detail of a vortex. Simulation parameters can be found in Table 2.

5.4 Richtmyer-Meshkov Instability (2D / 2D)

To conclude this section, we study the Richtmyer-Meshkov instability. This is a phenomenon which takes place when the perturbed interface between a thin and a dense gas is momentarily accelerated by a passing shock. The misalignment of the pressure gradient (due to the shock) and the density gradient induces vorticity, which leads to the formation of a mushroom-like interface[4]. A more detailed physical background, as well as experimental images, can be found in [2]. This instability has been used to validate a lattice-Boltzmann method in [52].

We shall consider two gases with mass ratio $m_2/m_1 = 5$ in a rectangular domain $\Omega = (-0.5, 0.5) \times (0, 0.5)$. The Knudsen number is here chosen as $\varepsilon = 10^{-6}$ in order to correctly resolve the instability. The gases are initially separate: the first (lighter) gas occupies the $x \leq b(y)$ region, with a perturbed boundary given by $x = -10^{-2}\sin(20\pi y)$, whereas the second (heavier) gas lies in the rest of the domain. The initial configuration of the first gas is a normal shock wave of Mach number $\mathrm{Ma} = 1.21$ (inspired by [52]) propagating in the positive x-direction. Its initial distribution is chosen according to the following Riemann datum:

$$\begin{cases} \rho_1 = 1.268, & \bar{v}_{1,x} = 0.256, & \bar{v}_{1,y} = 0, & p_1 = 0.809, & \text{if } x \leq s_0; \\ \rho_1 = 1, & \bar{v}_{1,x} = 0, & \bar{v}_{1,y} = 0, & p_1 = 0.5, & \text{if } x > s_0; \end{cases}$$

s_0, the initial position of the shock, is a negative constant. The second gas is initially stationary, with density $\rho_2 = 5$, and pressure $p_2 = 0.5$ to ensure the boundary is initially not forced. The initial distribution of the gases are the Maxwellians corresponding to these moments. For convenience, in order to avoid the interface leaving the domain, all the horizontal velocities are decreased by 7×10^{-2}.

[4]This instability is not to be confused with the related Rayleigh-Taylor instability, which arises on a perturbed interface when the dense gas is accelerated continuously by the thin gas, rather than by a shock. More details as well as experimental images can be found in [58]

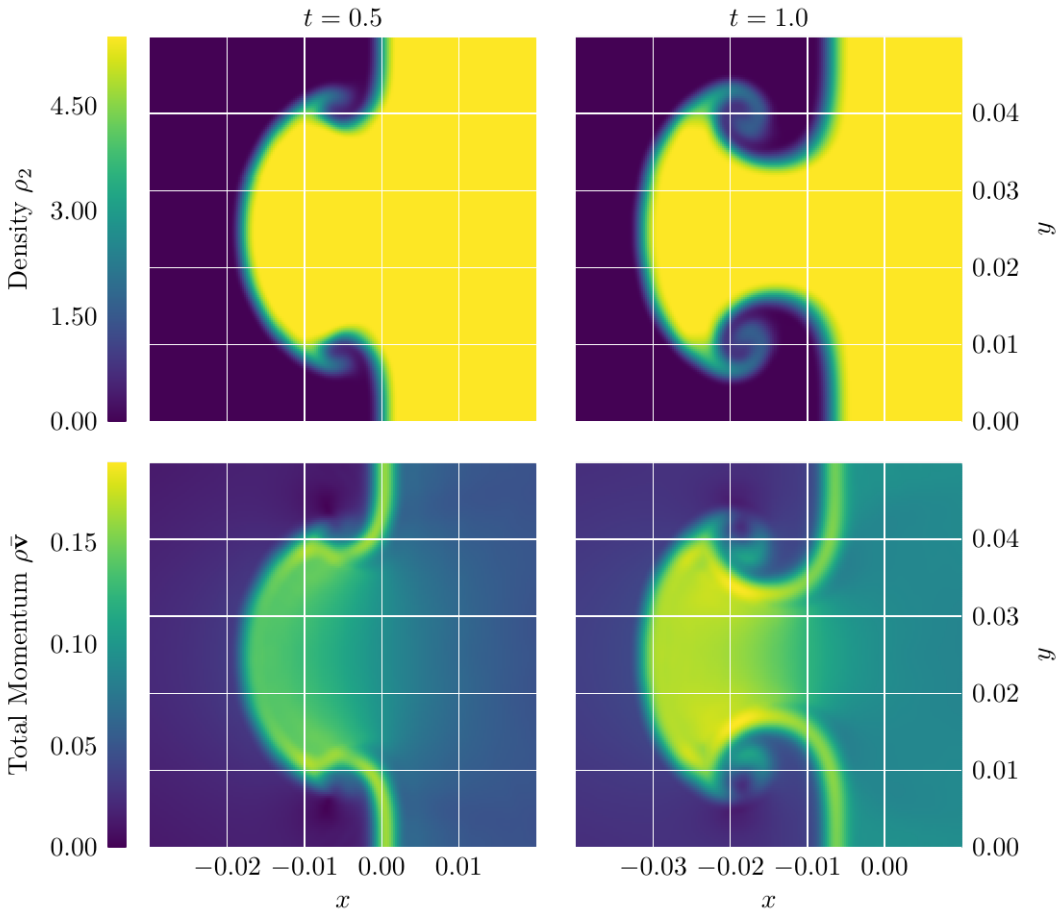

Figure 13: Richtmyer-Meshkov instability: density of the second species and modulus of the total momentum. **Left**: after the initial shock interaction, vortices arise. **Right**: the interface is deformed into a mushroom-like shape. Simulation parameters can be found in Table 3.

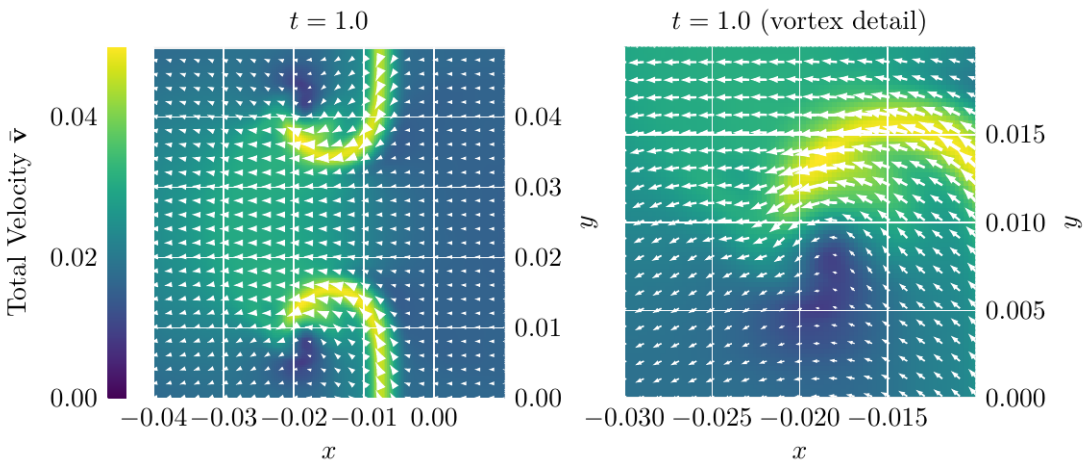

Figure 14: Richtmyer-Meshkov instability: modulus of the total velocity $\bar{\mathbf{v}}$ and stream lines at the final time. **Left**: whole domain. **Right**: detail of the lower vortex. Simulation parameters can be found in Table 3.

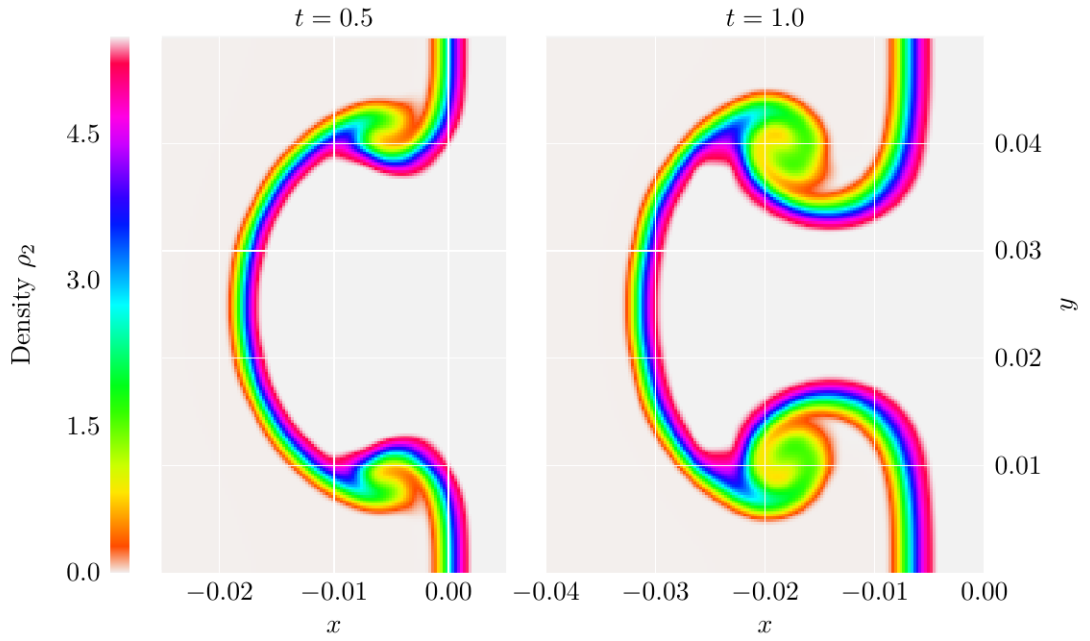

Figure 15: Richtmyer-Meshkov instability: detail of the gas interface (density of the second species). **Left**: vortices appear. **Right**: mushroom-like interface is formed. Simulation parameters can be found in Table 3.

Numerically, the domain Ω is discretised with $\Delta x = \Delta y = 2.5 \times 10^{-4}$ (400×200 cells). The velocity space is set as $(-4, 4)^2$, with $\Delta v = 2.5 \times 10^{-1}$ (32^2 cells). In total, the phase space is discretised with 81,920,000 cells. We impose outflow boundary conditions.

The solution is computed over the time $t \in (-0.02, 1.0)$. We choose the negative initial time and let $s_0 = 2.42 \times 10^{-2}$ so that the shock crosses the $x = 0$ line exactly at $t = 0$. We employ the telescopic two-level method, with step sizes $\Delta t_0 = 5 \times 10^{-7}$, $\Delta t_1 = 2 \times 10^{-6}$, and $\Delta t_2 = 6.25 \times 10^{-5}$, and inner steps $K_0 = 1$ and $K_1 = 6$. Once more, the inner steps follow the pattern $4\Delta t_0 = 2\varepsilon = \Delta t_1$ and the outermost step is restricted by the hyperbolic CFL condition. The use of telescopic projective integration decreases the computational cost by a factor of $S \simeq 9$, as defined in Eq. (3.8).

Figure 13 shows the density of the heavier gas and the modulus of the total momentum of the system at two different times. The gas interface is seen deforming as it develops a mushroom-like shape. Vortices are visible on either side of the perturbation, and much of the system's momentum is found at the interface.

Figure 14 studies the vortices at the final simulation time. The figure shows the modulus of the total velocity with streamlines, detailing the high speed along the lateral gas interface, and offering a magnified view of the lower vortex.

Figure 15 offers a detailed view of the gas interface. The density of the heavier gas has been recoloured to omit the extrema, highlighting only the density gradient. The vortex formation and the deformation of the interface are particularly clear here.

A summary of the simulation parameters can be found in Table 3.

Appendix: Solving the Sod Tube Problem

We recall, for the sake of a complete exposition, the solution to the classical Sod Tube problem and its generalisation to the two fluid setting, as can be found in the literature of hyperbolic problems [42]. In the usual setting, the initial Riemann datum is given by the left $(\rho_L, v_L, \mathcal{P}_L)$ and right $(\rho_R, v_R, \mathcal{P}_R)$ states:

$$\begin{cases} \rho = \rho_L, & v = v_L, & \mathcal{P} = \mathcal{P}_L, & \text{if } x \leq 0; \\ \rho = \rho_R, & v = v_R, & \mathcal{P} = \mathcal{P}_R, & \text{if } x > 0. \end{cases}$$

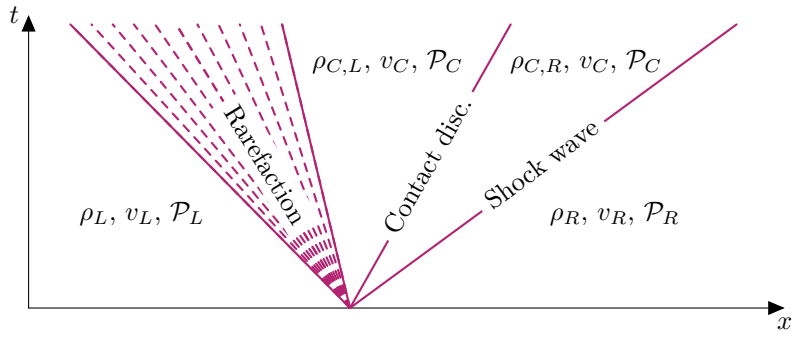

Figure 16: Structure of the solution to the Sod Tube problem

As the datum evolves, typically we observe two non-linear waves enveloping a new central region; see Fig. 16 for a diagram. This region comprises two states, separated by a contact discontinuity. Both have equal speed and pressure, v_C, $\mathcal{P}_C$, but different densities, $\rho_{C,L}$, and $\rho_{C,R}$. We will assume here $\mathcal{P}_L \geq \mathcal{P}_C \geq \mathcal{P}_R$, meaning the leftmost wave is a rarefaction, and the rightmost wave is a shock.

The solution strategy involves first finding values v_C, $\mathcal{P}_C$ which are consistent with the rarefaction/shock wave structure on either side. Given a guess for $\mathcal{P}_C$, the value of v_C can be computed from the left state using the *Riemann invariants* (quantities which are constant across the rarefaction). The precise relation is

$$v_{\text{rare}}(\mathcal{P}_C) = v_L + 2c_L\left[1 - \left(\frac{\mathcal{P}_C}{\mathcal{P}_L}\right)^{\frac{\gamma-1}{2\gamma}}\right](\gamma-1)^{-1},$$

where c_L is the speed of sound on the left state, computed via $c = \sqrt{\gamma\mathcal{P}/\rho}$, and where γ is the *adiabatic exponent*; for an ideal monatomic gas, it is given by $\gamma = 1 + 2/D$, where D is the dimension. Similarly, the value of v_C can be computed from the right state using the *Rankine-Hugoniot conditions*, which relate the quantities on either side of the shock. In this case, the expression is

$$v_{\text{shock}}(\mathcal{P}_C) = v_R + 2c_R\left(1 - \frac{\mathcal{P}_C}{\mathcal{P}_R}\right)\left[2\gamma\left(\gamma - 1 + \frac{\mathcal{P}_C(\gamma+1)}{\mathcal{P}_R}\right)\right]^{-\frac{1}{2}}.$$

A suitable value of $\mathcal{P}_C$ can thus be found by solving $v_{\text{rare}}(\mathcal{P}_C) = v_{\text{shock}}(\mathcal{P}_C)$. This determines the value of v_C also. Having established these, the densities on either side of the contact discontinuity are found as

$$\rho_{C,L} = \rho_L\left(\frac{\mathcal{P}_C}{\mathcal{P}_L}\right)^{\frac{1}{\gamma}}, \quad \rho_{C,R} = \rho_R\left(\frac{\mathcal{P}_C}{\mathcal{P}_R} + \frac{\gamma-1}{\gamma+1}\right)\left(\frac{\mathcal{P}_C(\gamma-1)}{\mathcal{P}_R(\gamma+1)} + 1\right)^{-1}.$$

A detailed derivation of these relations can be found in [55], for instance.

We now proceed to establish the spatial structure of the solution. The rarefaction, contact discontinuity, and shock wave all radiate from the initial point of discontinuity. The head and the tail of the rarefaction radiate at speeds $v_L - c_L$ and $v_C - c_C$ respectively. The contact discontinuity travels at speed v_C. Lastly, the shock propagates at speed $s = \frac{\rho_R v_R - \rho_{C,R} v_C}{\rho_R - \rho_{C,R}}$. These four speeds and their associated trajectories partition space into five intervals. The solution is constant inside each interval, except inside the rarefaction wave, where it takes the form:

$$\begin{aligned} v_{\text{rare}}(\xi) &= [(\gamma-1)v_L + 2(c_l + \xi)](\gamma+1)^{-1}, & c_{\text{rare}}(\xi) &= v_{\text{rare}}(\xi) - \xi, \\ \rho_{\text{rare}}(\xi) &= \left[\rho_L^{\gamma} c_{\text{rare}}^2(\xi)(\gamma\mathcal{P}_L)^{-1}\right]^{\frac{1}{\gamma-1}}, & \mathcal{P}_{\text{rare}}(\xi) &= \rho_{\text{rare}}^{\gamma}(\xi)\mathcal{P}_L\rho_L^{-\gamma}, \end{aligned}$$

where $\xi = x/t$. In summary, at time t and position x, the solution takes the form

$$\begin{cases} \rho = \rho_L, & v = v_L, & \mathcal{P} = \mathcal{P}_L, & \text{if } \xi \leq v_L - c_L; \\ \rho = \rho_{\text{rare}}(\xi), & v = v_{\text{rare}}(\xi), & \mathcal{P} = \mathcal{P}_{\text{rare}}(\xi), & \text{if } v_L - c_L \leq \xi \leq v_C - c_C; \\ \rho = \rho_{C,L}, & v = v_C, & \mathcal{P} = \mathcal{P}_C, & \text{if } v_C - c_C \leq \xi \leq v_C; \\ \rho = \rho_{C,R}, & v = v_C, & \mathcal{P} = \mathcal{P}_C, & \text{if } v_C \leq \xi \leq s; \\ \rho = \rho_R, & v = v_R, & \mathcal{P} = \mathcal{P}_R, & \text{if } s \leq \xi. \end{cases}$$

A two fluid Sod Tube problem can be constructed by considering two initially separate fluids, in contact at the point $x = 0$; the left fluid with state $(\rho_L, v_L, \mathcal{P}_L)$, and the right fluid with state $(\rho_R, v_R, \mathcal{P}_R)$. This datum generates a solution profile which is identical to the one described above, and the two fluids simply remain unmixed, separated by the contact discontinuity [42]. This is true even if the fluids have different adiabatic exponents, in which case the solution is calculated by using γ_L and γ_R respectively left and right of the contact discontinuity.

References

[1] A. Alaia, S. Pieraccini, and G. Puppo. Velocity Discretization in Numerical Schemes for BGK Equations. In S. Benzoni-Gavage and D. Serre, editors, *Hyperbolic Problems: Theory, Numerics, Applications*, pages 857–864. Springer Berlin Heidelberg, Berlin, Heidelberg, 2008.

[2] R. Aure and J. W. Jacobs. Particle image velocimetry study of the shock-induced single mode Richtmyer–Meshkov instability. *Shock Waves*, 18(3):161–167, Aug. 2008.

[3] F. Bernard, A. Iollo, and G. Puppo. BGK Polyatomic Model for Rarefied Flows. *J. Sci. Comput.*, 78(3):1893–1916, Mar. 2019.

[4] P. L. Bhatnagar, E. P. Gross, and M. Krook. A Model for Collision Processes in Gases. I. Small Amplitude Processes in Charged and Neutral One-Component Systems. *Phys. Rev.*, 94(3):511–525, May 1954.

[5] G. A. Bird. *Molecular Gas Dynamics and the Direct Simulation of Gas Flows*. Number 42 in Oxford Engineering Science Series. Clarendon Press ; Oxford University Press, Oxford : New York, 1994.

[6] M. Bisi, A. V. Bobylev, M. Groppi, and G. Spiga. Hydrodynamic equations from a BGK model for inert gas mixtures. In *31st International Symposium on Rarefied Gas Dynamics*, Glasgow, UK, 2019.

[7] A. Bondesan, L. Boudin, and B. Grec. A numerical scheme for a kinetic model for mixtures in the diffusive limit using the moment method. *Numer. Meth. Part. Differ. Equat.*, 35(3):1184–1205, 2019.

[8] M. Briant. étude des gaz multi-espèces proches de l'équilibre. *Séminaire L. Schwartz*, pages 1–17, 2015.

[9] M. Briant. Stability of global equilibrium for the multi-species Boltzmann equation in L^∞ settings. *DCDS-A*, 36:6669–6688, Oct. 2016.

[10] M. Briant and E. S. Daus. The Boltzmann Equation for a Multi-species Mixture Close to Global Equilibrium. *Arch. Ration. Mech. Anal.*, 222(3):1367–1443, Dec. 2016.

[11] S. Brull and C. Prigent. Local Discrete Velocity Grids for Multi-Species Rarefied Flow Simulations. *Commun. Comput. Phys.*, 28(4):1274–1304, June 2020.

[12] C. Buet. A discrete-velocity scheme for the Boltzmann operator of rarefied gas dynamics. *Transport Theor. Stat.*, 25(1):33–60, Jan. 1996.

[13] Z. Cai and R. Li. Numerical Regularized Moment Method of Arbitrary Order for Boltzmann-BGK Equation. *SIAM J. Sci. Comput.*, 32(5):2875–2907, Jan. 2010.

[14] C. Cercignani. *The Boltzmann Equation and Its Applications*, volume 67 of *Applied Mathematical Sciences*. Springer New York, New York, NY, 1988.

[15] C. Cercignani. Are there more than five linearly-independent collision invariants for the Boltzmann equation? *J. Stat. Phys.*, 58(5-6):817–823, Mar. 1990.

[16] C. Cercignani, R. Illner, and M. Pulvirenti. *The Mathematical Theory of Dilute Gases*, volume 106 of *Applied Mathematical Sciences*. Springer New York, New York, NY, 1994.

[17] S. Chapman and T. G. Cowling. *The Mathematical Theory of Non-Uniform Gases: An Account of the Kinetic Theory of Viscosity, Thermal Conduction, and Diffusion in Gases*. Cambridge Mathematical Library. Cambridge University Press, Cambridge ; New York, 3rd ed edition, 1990.

[18] N. Crouseilles, M. Mehrenberger, and E. Sonnendrücker. Conservative semi-Lagrangian schemes for Vlasov equations. *J. Comput. Phys.*, 229(6):1927–1953, Mar. 2010.

[19] N. Crouseilles, T. Respaud, and E. Sonnendrücker. A forward semi-Lagrangian method for the numerical solution of the Vlasov equation. *Comput. Phys. Commun.*, 180(10):1730–1745, Oct. 2009.

[20] E. S. Daus, A. Jüngel, C. Mouhot, and N. Zamponi. Hypocoercivity for a Linearized Multispecies Boltzmann System. *SIAM J. Math. Anal.*, 48(1):538–568, Jan. 2016.

[21] R. Dillman and J. Corliss. Overview of the Mars sample return Earth entry vehicle. In *Sixth International Planetary Probe Workshop*, 2008.

[22] G. Dimarco, R. Loubère, J. Narski, and T. Rey. An efficient numerical method for solving the Boltzmann equation in multidimensions. *J. Comput. Phys.*, 353:46–81, Jan. 2018.

[23] G. Dimarco and L. Pareschi. Numerical methods for kinetic equations. *Acta Numer.*, 23:369–520, May 2014.

[24] R. S. Ellis and M. A. Pinsky. The first and second fluid approximations to the linearized Boltzmann equation. *J. Math. Pures Appl.*, 54(9):125–156, 1975.

[25] B. Engquist, X. Li, W. Ren, E. Vanden-Eijnden, and E. Weinan. Heterogeneous multiscale methods: A review. *Commun. Comput. Phys.*, 2(3):367–450, 2007.

[26] F. Filbet and T. Rey. A rescaling velocity method for dissipative kinetic equations. Applications to granular media. *J. Comput. Phys.*, 248:177–199, Sept. 2013.

[27] I. Gallagher, L. Saint-Raymond, and B. Texier. *From Newton to Boltzmann: Hard Spheres and Short-Range Potentials*. Zurich Lectures in Advanced Mathematics. European Mathematical Society, Zürich, Switzerland, 2013.

[28] C. W. Gear, J. M. Hyman, P. G. Kevrekidid, I. G. Kevrekidis, O. Runborg, and C. Theodoropoulos. Equation-Free, Coarse-Grained Multiscale Computation: Enabling Mocroscopic Simulators to Perform System-Level Analysis. *Commun. Math. Sci.*, 1(4):715–762, Dec. 2003.

[29] C. W. Gear and I. G. Kevrekidis. Projective Methods for Stiff Differential Equations: Problems with Gaps in Their Eigenvalue Spectrum. *SIAM J. Sci. Comput.*, 24(4):1091–1106, Jan. 2003.

[30] C. W. Gear and I. G. Kevrekidis. Telescopic projective methods for parabolic differential equations. *J. Comput. Phys.*, 187(1):95–109, May 2003.

[31] J. R. Haack, C. D. Hauck, and M. S. Murillo. A Conservative, Entropic Multispecies BGK Model. *J. Stat. Phys.*, 168(4):826–856, Aug. 2017.

[32] J. Hu, S. Jin, and Q. Li. Asymptotic-Preserving Schemes for Multiscale Hyperbolic and Kinetic Equations. In *Handbook of Numerical Analysis*, volume 18, pages 103–129. Elsevier, 2017.

[33] S. Jin. Efficient Asymptotic-Preserving (AP) Schemes For Some Multiscale Kinetic Equations. *SIAM J. Sci. Comput.*, 21(2):441–454, Jan. 1999.

[34] S. Jin. Asymptotic preserving (AP) schemes for multiscale kinetic and hyperbolic equations: A review. *Riv. Mat. Univ. Parma*, 3:177–216, 2012.

[35] T. Kataoka, M. Tsutahara, K. Ogawa, Y. Yamamoto, M. Shoji, and Y. Sakai. Knudsen Pump and Its Possibility of Application to Satellite Control, 2004.

[36] J. Koellermeier and G. Samaey. Projective Integration for Moment Models of the BGK Equation. In V. V. Krzhizhanovskaya, G. Závodszky, M. H. Lees, J. J. Dongarra, P. M. A. Sloot, S. Brissos, and J. Teixeira, editors, *Computational Science – ICCS 2020*, volume 12142, pages 321–333. Springer International Publishing, Cham, 2020.

[37] P. Lafitte, A. Lejon, and G. Samaey. A High-Order Asymptotic-Preserving Scheme for Kinetic Equations Using Projective Integration. *SIAM J. Numer. Anal.*, 54(1):1–33, Jan. 2016.

[38] P. Lafitte, W. Melis, and G. Samaey. A high-order relaxation method with projective integration for solving nonlinear systems of hyperbolic conservation laws. *J. Comput. Phys.*, 340:1–25, July 2017.

[39] P. Lafitte and G. Samaey. Asymptotic-preserving Projective Integration Schemes for Kinetic Equations in the Diffusion Limit. *SIAM J. Sci. Comput.*, 34(2):A579–A602, Jan. 2012.

[40] S. L. Lee and C. W. Gear. Second-order accurate projective integrators for multiscale problems. *J. Comput. Appl. Math.*, 201(1):258–274, Apr. 2007.

[41] R. J. LeVeque. *Numerical Methods for Conservation Laws*, volume 57. Birkhäuser Basel, Basel, 1990.

[42] R. J. LeVeque. *Finite Volume Methods for Hyperbolic Problems*. Cambridge University Press, Cambridge, 2002.

[43] X.-D. Liu, S. Osher, and T. Chan. Weighted Essentially Non-oscillatory Schemes. *J. Comput. Phys.*, 115(1):200–212, Nov. 1994.

[44] C. P. McNally, W. Lyra, and J.-C. Passy. A Well-Posed Kelvin-Helmholtz Instability Test and Comparison. *ApJS*, 201(2):18, Aug. 2012.

[45] W. Melis, T. Rey, and G. Samaey. Projective Integration for Nonlinear BGK Kinetic Equations. In C. Cancès and P. Omnes, editors, *Finite Volumes for Complex Applications VIII - Hyperbolic, Elliptic and Parabolic Problems*, volume 200, pages 145–153. Springer International Publishing, Cham, 2017.

[46] W. Melis, T. Rey, and G. Samaey. Projective and telescopic projective integration for the nonlinear BGK and Boltzmann equations. *SMAI J. Comput. Math.*, 5:53–88, 2019.

[47] W. Melis and G. Samaey. Telescopic Projective Integration for Linear Kinetic Equations with Multiple Relaxation Times. *J. Sci. Comput.*, 76(2):697–726, Aug. 2018.

[48] L. Mieussens. Discrete Velocity Model and Implicit Scheme for the BGK Equation of Rarefied Gas Dynamics. *Math. Models Methods Appl. Sci.*, 10(08):1121–1149, Nov. 2000.

[49] T. Rey. A Spectral Study of the Linearized Boltzmann Equation for Diffusively Excited Granular Media. *arXiv:1310.7234*, Oct. 2013.

[50] R. Rico-Martínez, C. Gear, and I. G. Kevrekidis. Coarse projective kMC integration: Forward/reverse initial and boundary value problems. *J. Comput. Phys.*, 196(2):474–489, May 2004.

[51] F. Rogier and J. Schneider. A direct method for solving the Boltzmann equation. *Transport Theor. Stat.*, 23(1-3):313–338, Jan. 1994.

[52] G. N. Sashi Kumar and N. K. Maheshwari. Viscous multi-species lattice Boltzmann solver for simulating shock-wave structure. *Comput. Fluids*, 203:104539, May 2020.

[53] G. A. Sod. A survey of several finite difference methods for systems of nonlinear hyperbolic conservation laws. *J. Comput. Phys.*, 27(1):1–31, Apr. 1978.

[54] H. Struchtrup. *Macroscopic Transport Equations for Rarefied Gas Flows: Approximation Methods in Kinetic Theory*. Interaction of Mechanics and Mathematics. Springer-Verlag, Berlin Heidelberg, 2005.

[55] E. F. Toro. *Riemann Solvers and Numerical Methods for Fluid Dynamics*. Springer Berlin Heidelberg, Berlin, Heidelberg, 1999.

[56] M. Torrilhon. Two-Dimensional Bulk Microflow Simulations Based on Regularized Grad's 13-Moment Equations. *Multiscale Model. Simul.*, 5(3):695–728, Jan. 2006.

[57] C. Villani. A Review of Mathematical Topics in Collisional Kinetic Theory. In *Handbook of Mathematical Fluid Dynamics*, volume 1, pages 71–74. Elsevier, 2002.

[58] J. T. Waddell, C. E. Niederhaus, and J. W. Jacobs. Experimental study of Rayleigh–Taylor instability: Low Atwood number liquid systems with single-mode initial perturbations. *Physics of Fluids*, 13(5):1263–1273, May 2001.

[59] L. Wu, J. Zhang, J. M. Reese, and Y. Zhang. A fast spectral method for the Boltzmann equation for monatomic gas mixtures. *J. Comput. Phys.*, 298:602–621, Oct. 2015.